Formation - Exhumation History of the Carboniferous Axi Epithermal Gold Deposit in the Chinese Western Tianshan Based on Zircon U-Pb and Pyrite Re - Os geochronology, and (U-Th)/He Zircon - Apatite Thermochronometry

Nuo Li [a, b, c*], Bo Zhang [d], Martin Danišík [e], Yan-Jing Chen [d], David Selby [f], Wenjiao Xiao [a, b, c]

[a] *Xinjiang Research Center for Mineral Resources, Xinjiang Institute of Ecology and Geography, Chinese Academy of Sciences, Urumqi 830011, China*

[b] *Xinjiang Laboratory of Mineral Resources and Digital Geology, Urumqi 830011, China*

[c] *Key Laboratory of Ecological Safety and Sustainable Development in Arid Lands, State Key Laboratory of Desert and Oasis Ecology, Xinjiang Institute of Ecology and Geography, Chinese Academy of Sciences, Urumqi 830011, China*

[d] *Key Laboratory of Orogen and Crust Evolution, Peking University, Beijing, 100871, China*

[e] *John de Laeter Centre, Curtin University, GPO Box U1987, Perth, WA 6845, Australia*

[f] *Department of Earth Sciences, University of Durham, Durham DH1 3LE, United Kingdom*

*Corresponding author. E–mail address: linuo@ms.xjb.ac.cn; nuolipku@126.com

ORCID: 0000-0002-0865-1065

Abstract

The Central Asian Orogenic Belt (CAOB) represents a Late Paleozoic archipelago. Yet the crustal growth, reworking and exhumation of individual microcontinental massifs remain poorly constrained. Here, we utilize the Axi epithermal deposit to examine continental preservation and exhumation of CAOB in the Chinese Western Tianshan. Zircon U-Pb dating and geochemistry demonstrate that the andesitic host rock formed by incremental addition of magma in an Andean-type magmatic arc setting at 362, 354 and 342 Ma. Pyrite Re-Os data and textural evidence reveal two mineralization events at 355 and 332 Ma. Zircon (U-Th)/He data reveal temperatures of ~180 °C until 317.8 ± 9.8 Ma, which is interpreted to record the timing of exhumation of the andesite and gold orebodies prior to their burial by Carboniferous aged sediments. Further sedimentary concealment continued until the Late Mesozoic, when the system was re-exhumed between 148.6 ± 8.6 and 120.0 ± 13 Ma at a rate of ~9.8 m/Ma as shown by apatite (U-Th)/He data . Collectively, the geo-/thermochronology demonstrates that the Chinese Western Tianshan records the transition from compressional to extensional tectonism during the Late Paleozoic and the Late Mesozoic. The shallow epithermal mineralization was protected from erosion by post-mineralization deposition.

Keywords: Chronology; Paleozoic epithermal deposit; Axi; Chinese Western Tianshan; Central Asian Orogenic Belt

The Central Asian Orogenic Belt (CAOB) lies between the Siberian Craton to the north and Tarim-North China Craton to the south and represents one of the largest and most long-lived accretionary orogens (Fig. 1a). The CAOB was produced by protracted amalgamation of multiple island arcs, oceanic islands, seamounts, accretionary wedges, oceanic plateau and microcontinents (Xiao et al., 2009). However, crustal growth, reworking and exhumation of individual microcontinental massifs, remain poorly constrained (see Dumitru et al., 2001; Glorie et al., 2010; Xiao et al., 2013, 2019 for details). Yet, the preservation of Paleozoic epithermal hydrothermal systems provides the opportunity to assess the preservation and exhumation of microcontinental massifs of the CAOB.

Epithermal deposits are attractive targets for gold and silver exploration worldwide. They mainly form in subaerial environments (at depths of <1.5 km) along convergent margin settings and are highly susceptible to erosion (White and Hedenquist, 1990; Cooke and Simmons, 2000; Simmons et al., 2005). Consequently, their preservation potential is poor in the geological record, and most epithermal deposits worldwide are of Mesozoic-Cenozoic age (Kesler and Wilkinson, 2006; Wilkinson and Kesler, 2007). However, within the CAOB, Paleozoic-aged epithermal deposits are prevalent (Chen et al., 2012). The preservation of these Paleozoic epithermal systems cannot be explained without understanding the processes generating the deposits and the preservation potential of their depositional environments.

In the Chinese Western Tianshan of the CAOB, the Axi deposit is the largest known low sulfidation epithermal gold deposit. Previous studies provide sufficient geological information to develop robust constraints on the sequence of events leading to deposit formation (Zhai et al., 2009; Liu et al., 2018, 2020; Zhang et al., 2018). Yet the post-mineralization history is poorly constrained, which has hampered a comprehensive understanding of the preservation of such an old epithermal deposit. Here we combine four dating techniques in order to unravel the temporal framework of magmatism (U-Pb on zircon), gold mineralization (Re-Os on pyrite) and the post-mineralization thermal history ((U-Th-[Sm])/He on zircon and apatite). The combination of the four dating techniques provides a thermal history over a temperature range of >700°C, and enables the reconstruction of the formation and exhumation of the Axi deposit, and by interpretation other region, temporally-related epithermal deposits/systems. Our work shows that this combination of geochronological methods is a powerful tool to yield critical temporal insights into crustal growth and exhumation of the Chinese Western Tianshan, as shown for other continental massifs (Reiners et al., 2006; Danišík et al., 2010; Spencer et al., 2019).

Geological background

Geology of the Chinese Western Tianshan

The Chinese Western Tianshan along the southern margin of CAOB (Fig. 1a) represents a Paleozoic orogenic collage that formed by multi-stage accretion and amalgamation of the Tarim and other micro-continental blocks (Xiao et al., 2009; Xiao and Kusky, 2009; Chen et al., 2012). Three suture zones, namely the North Tianshan Suture, the Nikolaev Line-North Nalati and the South Tianshan (or South Central Tianshan) suture zones, further divide the Chinese Western Tianshan into four tectonic units, i.e., the North, Central and South Tianshan and the Yili Block (Gao et al., 2009, Fig. 1b). The North Tianshan is a Paleozoic accretionary complex consisting of a west-northwest striking ophiolitic mélange zone due to the southward subduction of the Junggar Ocean (Xiao et al. 2013). One of the best-preserved units – the Bayingou ophiolite, contains Upper

Devonian – Lower Carboniferous radiolaria and conodonts microfossils, ophiolitic olivine clinopyroxenites, gabbro cumulates and sheeted dykes that are all thrust onto sequences of tholeiitic basalt (Wang et al., 1990). One gabbro sample dated at 344.0 ± 3.4 Ma by zircon U-Pb was intruded by a plagiogranite dated to 324.7 ± 7.1 Ma (Xu et al., 2006). The Yili Block is a triangular-shaped microcontinent situated between the North and Central Tianshan and becomes narrower to the east. The Yili Block is mainly composed of Paleoproterozoic to Neoproterozoic high-grade metamorphic rocks, upper Neoproterozoic to Lower Paleozoic passive margin sediments, Upper Ordovician-Silurian granite, and Devonian to Carboniferous - Lower Permian volcanic and clastic sedimentary rocks (An et al., 2013; Zhao et al., 2014b). The lens-shaped Central Tianshan is underlain by Meso-Neoproterozoic aged basement, which is composed of sillimanite-biotite-quartz schist, garnet-plagioclase-granulite, gneisses, amphibolites, migmatite and marbles (Wang et al., 1990). The basement was covered by Ordovician-Silurian meta-volcano-sedimentary rocks and Carboniferous-Permian sedimentary rocks that underwent greenschist- to amphibolite-facies and locally granulite facies metamorphism (Zhu et al., 2009). The South Tianshan is a Paleozoic accretionary complex resulting from the closure of the South Tianshan Ocean followed by collision between the Tarim Craton and the Yili Block (Kröner et al., 2013). The principal outcropping strata are Paleozoic siliciclastic turbidite, limestone, chert and schist that were previously assigned to having a passive margin affinity (Han et al., 2011). However, more recently, an oceanic plate affinity has been recognized for the Silurian to Carboniferous strata (Safonova et al., 2016). The ophiolitic mélange, dated at 500 – 332 Ma (Jiang et al., 2014), is present as exotic slices in the Paleozoic strata and is, in part, affected by Late Paleozoic or Triassic high/ultra-high-pressure metamorphism (Xiao et al., 2013, 2019 and references therein).

The Tulasu district hosting the Axi deposit is a WNW-trending graben basin situated in the northeastern part of the Yili Block. The basin was developed on the Proterozoic and lower Paleozoic basement (Zhao et al., 2020). The Proterozoic basement is dominated by shallow marine carbonate interlayered with siltstone, and the lower Paleozoic rocks comprising Ordovician to Silurian limestone, sandstone, siltstone with minor interlayered volcanic rocks (Dong and Sha, 2005; Zhai et al., 2009, Fig. 2). These rocks are unconformably overlain by the Lower Devonian Tulasu Formation, a terrigenous sequence of conglomerate, pebbly sandstone and siltstone. The Devonian-Carboniferous Dahalajunshan Formation covers nearly half of the basin and hosts numerous gold (e.g., Axi, Jingxi-Yelmand; Zhang et al., 2018; Ye et al., 2020) and Pb-Zn deposits (e.g., Tabei, Tulasu; Peng et al., 2018). The Dahalujunshan Formation extrusive rocks have a total thickness of 1070–4500 m and consist mainly of intermediate to acid volcanic-sedimentary rocks. Five lithological units have been distinguished from bottom to top (Unit 1 to 5 in Fig. 2), named the Conglomerate Member, the Acid Tuff Member, the Lower Andesite Member, the Volcaniclastic Member and the Upper Andesite Member, respectively (Zhai et al., 2009). The Dahalajunshan Formation is in turn overlain by a sequence of conglomerate, limestone and calcareous sandstone of the Lower Carboniferous Aqialehe Formation (Fig. 2). The Aqialehe Formation then gives way to Upper Carboniferous volcano-sedimentary rocks of the Naogaitu and Oyimanbulake formations. Further to the south, the cover includes: the Triassic Xiaoquangou Group sandstone, siltstone and pelite; Jurassic conglomerate, sandstone, pelite and coal bed; Tertiary conglomerate, sandstone, and pelite; and Quaternary sediments (Feng et al., 2000).

Geology of the Axi Deposit

The Axi deposit has a proven gold resource of 70 t (with an average grade of 5.6 g/t; Chen et al., 2012). It is hosted by andesitic to dacitic tuff, breccia and lava, belonging to the youngest “upper andesite member” of the Dahalajunshan Formation (Unit 5 in Fig. 2). Based on detailed geological mapping, Dong and Sha (2005) proposed that, to the west of the annular fault (No. F2 in Fig. 3), the rocks are mainly explosive and overflow facies, whereas to the east, they are dominated by breccia and subvolcanic rocks. The Aqialehe Formation conglomerates and calcareous sandstones unconformably overlie the Dahalajunshan Formation. It contains Visean-aged fossils (e.g., *Siphonodendron sp., Caninia sp., Gigantoproductus sp.*; Zhai et al., 2009), thus the deposition age should be no later than 331 Ma (minimum for Visean as suggested by International Commission on Stratigraphy, 2020).

A suite of annular and radial faults is related to an oval shaped caldera (2.6 km × 2.4 km), as revealed by aeromagnetic mapping (Dong and Sha, 2005). The annular fault F2 and some radial faults (such as F4, F15 and F16) were then crosscut by the NW-trending fault F3 (Fig. 3a). To date, eight epithermal gold orebodies have been distinguished, with most occurring in the hanging wall of F2. The No. 1 orebody is the largest, contributing ~90 % of the total gold reserve. It extends along strike for more than 1000 m, with a thickness of >40 m and depth of >450 m. The average ore grade is 5.57 g/t Au and 11.02 g/t Ag (Chen et al., 2012). Detailed alteration and mineralization features have been provided by Zhai et al. (2009), An and Zhu (2018), Liu et al. (2018, 2020) and Zhang et al. (2018) – a brief summary is presented below. The deposit exhibits a zonal alteration distribution. Silicification dominants the central part of the orebody and is expressed by the occurrence of abundant quartz and/or chalcedony and is closely associated with gold mineralization. Upward and outward from the silicified zone is a zone of phyllic (Zhai et al., 2009; Liu et al., 2020) or sericitic alteration (An and Zhu, 2018). It is characterized by the occurrence of sericite, quartz and adularia, plus minor illite and carbonate. Encompassing the phyllic/sericitic zone is a peripheral propylitic zone that is >500 m wide and comprises an assemblage of chlorite, carbonate, and epidote. Gold occurs as native gold, electrum, or invisible gold hosted by pyrite and arsenopyrite (Liu et al., 2018; Zhang et al., 2018; Li et al., 2023). Other ore minerals include marcasite, sphalerite, chalcopyrite, tetrahedrite and galena.

It is noteworthy that, besides epithermal gold mineralization, the overlying Aqialehe Formation comprises a "basal conglomerate/Placer-style" gold orebody (Dong and Sha, 2005; Zhai et al., 2009). The placer-type Au deposit contains numerous angular or subangular gravels derived from auriferous quartz veins.

Previous chronological data of Axi

The eruption age of the andesite host was first established by Rb-Sr and $^{40}Ar/^{39}Ar$ dating on whole rock samples collected from drill cores to the east of F2 (Table 1). The pioneering work by Li et al. (1998) reported a well-defined $^{40}Ar/^{39}Ar$ plateau age of 325.1 ± 0.6 Ma for a pyroxene andesite, slightly younger than whole rock Rb-Sr isochron age of 345.9 ± 9 Ma. More recently, the emplacement age of the andesitic rocks has been dated by zircon SHRIMP and LA-ICPMS U-Pb methodologies (Zhai et al., 2006; An et al., 2013; Yu et al., 2016). The reported ages vary considerably from 351.1 ± 1.8 to 376 ± 3.1 Ma (Table 1). These studies, however, made a very simplistic assumption that all zircons present are autocrystic grains crystallized from the host magma. Given that inherited, antecrystic and xenocrystic zircon or zircon domains can yield significantly older age information, it is critical to distinguish them confidently from autocrystic grains (Miller et al., 2007; Siégel et al. 2018), in order to constrain the best estimate of emplacement age of the andesite.

The gold mineralization age was first constrained by Rb-Sr dating of fluid inclusions. Obtained results range from 301 ± 29 Ma to 339 ± 28 Ma (Li et al., 1998). Subsequently, An and Zhu (2018) reported K–Ar ages of 286.0 ± 7.4 to 292.7 ± 7.9 Ma for four auriferous whole rock samples and a Re-Os isochron pyrite age of 299 ± 35 Ma (MSWD = 0.55), which resulted in the interpretation of an Early Permian alteration-mineralization event. However, such a conclusion contradicts the fact that there is a pronounced angular unconformity between the epithermal orebody and the overlying Visean-aged Aqialehe Formation. Recently, Liu et al. (2020) identified two episodes of pyrite mineralization by combined Re-Os dating, sulfur isotope and trace elements data. The disseminated pyrite associated with pyrite-sericite-quartz alteration yielded a Re-Os isochron age of 353 ± 6 Ma (with an initial $^{187}Os/^{188}Os$ ratio of 0.11 ± 0.02). In contrast, fine-grained, oscillatory zoned pyrite from a gray quartz vein yielded a younger Re-Os isochron age of 332 ± 8 Ma (with an initial $^{187}Os/^{188}Os$ ratio of 0.17 ± 0.02). Compositionally, the older pyrite grains contain higher Cu, Co, Ni and V contents as well as $\delta^{34}S$ values (+2.9 to +4.0‰) in comparison with the younger, fine-grained pyrite ($\delta^{34}S$ = -0.10 to +3.1‰). Integrating geological, geochemical and isotopic signatures with nearby porphyry-epithermal deposits, the authors proposed a two-stage gold mineralization model: an earlier porphyry Cu ± Au mineralization at 356–353 Ma, and a later epithermal Au mineralization at ca. 332 Ma.

Sampling and Analytical methods

Samples

Four andesitic samples (AX-39, AX-S, AX-S5, AX-S41) were collected from surface outcrops

(Fig. 3a, Table 2) for zircon U-Pb geochronology, and zircon/apatite (U-Th-[Sm])/He thermochronology. The samples are located on the footwall of F2, within a horizontal distance of 850 m and an altitude variation of 300 m (from 1295 to 1600 m above sea level). The andesitic samples have a typical phyric texture where large plagioclase, clinopyroxene, amphibole and/or quartz phenocrysts are embedded in a microcrystalline groundmass of plagioclase, magnetite and ilmenite. They are further grouped according to the dominant phenocrysts, namely pyroxene andesite (sample AX-S5, containing clinopyroxene + plagioclase ± amphibole ± quartz phenocryst), amphibole andesite (sample AX-S, containing amphibole + plagioclase phenocryst), quartz andesite (sample AX-39, containing plagioclase + quartz ± amphibole phenocryst) and andesite (sample AX-S41, containing plagioclase phenocryst). The andesitic rocks are relatively fresh, without obvious hydrothermal alteration of the phenocrysts. The major and trace element compositions of the four samples are reported by Zhang (2020).

Four auriferous pyrite specimens (SBY-1, SBY-2, SBY-3, SBY-4) were extracted from the northern area (at elevations of 1300 – 1400 m above sea level) of the No.1 orebody for Re-Os isotope analysis. They belong to the earliest auriferous pyrite generation (Py1), which can be cemented by later auriferous, oscillatory zoned pyrite (Py3, aged 332 ± 8 Ma, Re-Os isochron; Liu et al., 2020) according to Zhang et al. (2018) and Zhang (2020). Eight marcasite samples (Mar1) postdating main gold mineralization were collected for Re-Os isotope analysis from five drill holes (ZK2404, ZK3605, ZK4004, ZK4007 and ZK4811).

Analytical methods

Zircon and apatite were separated by standard magnetic and heavy liquid separation techniques, and then handpicked under a binocular microscope. Selected zircon grains were mounted on epoxy and polished to expose their cores for further analysis. Cathodoluminescence (CL) imaging and zircon U-Pb dating were conducted at the State Key Laboratory of Continental Dynamics in the Northwest University (Xi'an, China). The CL imaging was carried out using a Quanta 400 FEG scanning electron microscope (SEM) with a MonoCL3+ cathodoluminescence spectroscope. LA-ICPMS zircon U-Pb dating and trace element analyses were synchronously carried out on an Agilent 7500a ICPMS coupled with Geolas 2005 laser ablation system equipped with a 193 nm ArF Excimer laser. For details, see Yuan et al. (2008). During the analyses, the laser spot diameter was 31 μm. Helium was used as carrier gas to enhance the transport efficiency of the ablated material. Standard zircons 91500, GJ-1, Monastery and NIST SRM 610 were used as external standards for calibration and for controlling the analytical conditions. The U, Th and Pb concentrations were calibrated using ^{29}Si as an internal standard and NIST SRM 610 as an external standard. Because of the high $^{206}Pb/^{204}Pb$ ratios (>1000), no correction for common-Pb was applied. The weighted mean U-Pb ages (with 95% confidence) and concordia diagrams were constructed using *IsoplotR* (Vermeesch, 2018).

The (U–Th)/He dating procedure followed the protocols described in Danišík et al. (2012). In brief, apatite and zircon crystals were photographed, measured, and transferred into platinum (apatite) and niobium (zircon) tubes. Helium (^{4}He) was extracted at ~950 °C (apatite) and ~1250 °C (zircon) under ultra–high vacuum using a diode laser and analyzed on the Helium extraction line at the John de Laeter Centre in Perth (Australia) using a Pfeiffer Prisma QMS–200 mass spectrometer. After the He measurements, Pt and Nb microtubes containing the crystals were retrieved from the Helium extraction line, spiked with ^{235}U and ^{230}Th, and dissolved in nitric acid (apatite) or in Parr acid digestions vessels (zircon) in two cycles of HF, HNO_3 (cycle 1), and HCl acids (cycle 2) following the procedures described in Evans et al. (2005). Sample, blank, and spiked standard solutions were then diluted by Milli-Q water and analyzed by isotope dilution for ^{238}U and ^{232}Th, and by external calibration for ^{147}Sm on an Element XR™ High Resolution ICP-MS. The total analytical uncertainty (TAU) was calculated as a square root of sum of squares of uncertainty on He and weighted uncertainties on U, Th, and Sm measurements. The raw (U-Th)/He ages were corrected for alpha ejection (Ft correction) after Farley et al. (1996), whereby homogenous distributions of U, Th, and Sm were assumed for the crystals. The accuracy of the (U-Th)/He dating procedure was monitored by replicate analyses of internal standards (Durango apatite and Fish Canyon Tuff zircon) where crystals measured over the course of this study yielded mean (U-Th)/He ages of 31.9 ± 2.1 Ma (95% conf. interval; n=4; Durango apatite) and 28.5 ± 1.8 Ma (95% conf. interval; n=3; Fish Canyon Tuff zircon, Table 3). These are in excellent agreement with the reference (U-Th)/He ages of 31.1 ± 1.0 Ma (Durango; McDowell et al., 2005) and 28.3 ± 1.3 Ma (Fish Canyon Tuff zircon; Reiners, 2005), respectively.

Sulfide Re-Os dating was performed at the Durham Geochemistry Center at the Department of Earth Sciences, University of Durham. For each analysis, 200–400 mg of pyrite/marcasite separate were weighed and transferred into a thick-walled borosilicate Carius tube (Shirey and Walker, 1995). Each aliquot was dissolved in inverse Aqua Regia (~3 mL of 11 N HCl and ~6 mL 16 N HNO_3) with a known amount of ^{185}Re + ^{190}Os tracer solution at 220 °C for 24 h (see Selby et al., 2009 for detail). In brief, following sample digestion, Os was isolated and purified using solvent extraction (CCl_3-HBr) and microdistillation (CrO_3-H_2SO_4-HBr), with the Re purified using solvent extraction (NaOH-C_3H_6O and anion chromatography. The Re and Os isotopic compositions were determined by negative thermal ionization mass spectrometry (N-TIMS) using a ThermoScientific Triton mass spectrometer at the Arthur Holmes Laboratory. Rhenium was measured as ReO_4^- in static mode on Faraday collectors, whereas Os was measured as OsO_3^- in peak-hopping mode on a SEM (Creaser et al., 1991; Völkening et al., 1991). As a monitor of measurement reproducibility in-house reference solutions of Re (125 pg aliquot – $^{185}Re/^{187}Re = 0.59892 \pm 0.00203$, n = 74) and Os (DROsS – 50 pg aliquot, $^{187}Os/^{188}Os = 0.160869 \pm 0.000410$, n = 100) are run. The analytical uncertainties result from full error propagation of weighing errors, spike calibration, standard measurements, mass spectrometry analyses and blanks. The Re-Os ages are determined through regression of Re-Os data in $^{187}Os/^{188}Os$ vs. $^{187}Re/^{188}Os$ space using 2σ level absolute uncertainties and the error correlation, rho, using *IsoplotR* (Vermeesch, 2018) with the ^{187}Re decay constant of Smoliar et al. (1996; $\lambda^{187}Re = 1.666e^{-11} \pm 5.165e^{-14}\ a^{-1}$). Alternatively, model Re-Os ages are obtained using the formula: $t = \ln[(^{187}Os^*/^{187}Re) + 1]/(\lambda^{187}Re)$, where $^{187}Os^*$ is the determined content of radiogenic ^{187}Os calculated using the initial $^{187}Os/^{188}Os$ value, plus its uncertainty, from regression of Re-Os data.

Dating and modeling results

Two types of zircon and their U-Pb ages

The zircon samples are divided in to two populations (groups) based on morphology, CL imaging and trace element characteristics. The first group, termed Zr1, is represented by anhedral crystals with simple or patched zonation or a wide overgrowth band (Fig. 4). The Zr1 zircons are common in the amphibole andesite (AX-S) and andesite (AX-S41), and occurs as zircon overgrowths or big grains (mostly >100 μm) with rounded surfaces and low length/width ratio (1.2 – 1.6). Prismatic or intact crystals are rare. In the pyroxene andesite (AX-S5) and quartz andesite

(AX-39), however, Zr1 is subordinate and mostly occurs as zircon cores bounded by truncation or resorption surfaces. The second group (termed as Zr2) is characterized by well-developed, fine-scale oscillatory zonation. The Zr2 group is common in the pyroxene andesite and quartz andesite, but absent in the amphibole andesite and andesite. More than 95 % of Zr2 occurs as an overgrowth around the distinct, anhedral Zr1 core. Occasionally, Zr2 is also presents as intact, euhedral to subhedral crystals (50 – 210 μm), with length/width ratios of 1.2 – 5.

Geochemically, Zr1 possesses higher Th/U (0.63 ± 0.09), but lower Hf (8230 ± 429 ppm), U (90 ± 19 ppm) and Th (55 ± 18 ppm) concentrations and $(Yb/Gd)_N$ (19 ± 3) in comparison with Zr2 (Th/U = 0.54 ± 0.05, Hf = 9248 ± 372 ppm, U = 157 ± 61 ppm, Th = 86 ± 37 ppm, $(Yb/Gd)_N$ = 24 ± 4) regardless of the age and host rock (Fig. 5, Table S1). Using the geothermometer proposed by Ferry and Watson (2007), and assuming a_{SiO2} constant at 1 and a_{TiO2} at 0.7, calculated zircon saturation temperatures of Zr1 (808 ± 36 °C) are higher than for Zr2 (756 ± 21 °C).

Zircon LA-ICPMS analyses yielded concordant, but highly dispersed ages (Table S2, Fig. 6a-d). Except for four old outliers aged 1693 ± 22 Ma ($^{207}Pb/^{206}Pb$ age), 435.8 ± 2.8 Ma, 380.4 ± 3.6 Ma and 377.3 ± 3.8 Ma, most $^{206}Pb/^{238}U$ ages group between 338 and 370 Ma. The U-Pb data for each sample, shown on a cumulative age plot (Fig. 6e), describes a continuous probability distribution, with Zr1 slightly older or contemporaneous with Zr2. The $^{206}Pb/^{238}U$ data are interpreted to yield the best estimate of the crystallization age of 355.3 ± 1.7 Ma for the quartz andesite (Fig. 6a), 354.3 ± 2.4 Ma for the andesite (Fig. 6b), 361.9 ± 1.8 Ma for the amphibole andesite (Fig. 6c) and 360.9 ± 2.1 Ma for the pyroxene andesite (Fig. 6d). The youngest age distribution patterns for each sample cluster around 342 Ma (Fig. 6).

Zircon and apatite (U–Th)/He data and thermal history modelling results

Twenty single-grain zircon (U-Th)/He (ZHe) dates were obtained for the four andesitic samples, with five dates determined for each sample (Table 3). Majority of ZHe dates is over-dispersed and anomalously old, possibly due to the intracrystalline complexities complicating alpha-ejection correction (Hourigan et al., 2005; Danišík et al., 2017) or He retained from pre-magmatic entrainment (Reiners et al., 2004). Using the youngest U-Pb age as a cut off, and also discarding one spuriously young outlier, the ZHe dates for the quartz andesite yield a tight cluster with the central value of 317.9 ± 9.8 Ma. The other three samples do not yield any reasonable ZHe ages.

Apatite (U-Th)/He (AHe) dates from 24 grains range from 87.6 ± 5.4 to 229.1 ± 25.6 Ma, and are systematically younger than the corresponding ZHe dates (Table 3). Given the lack of correlation between AHe dates and other parameters such as grain sizes and eU (Shuster et al. 2006; Flowers et al. 2009), the scatter and the "too old" ages are attributed to "parentless" He due to U-Th rich mineral inclusions. Excluding the "too old" ages, other data yield central values of 148.6 ± 8.6 Ma for the quartz andesite, 130.8 ± 4.7 Ma for the andesite, 124.0 ± 12 Ma for the amphibole andesite, and 120.0 ± 13.0 Ma for the pyroxene andesite. Within the limited sample profile, the central ages increase systematically with elevation (Fig. 7).

Sulfide Re-Os geochronology

The four pyrite samples analyzed possess between 5.56 ± 0.02 and 7.53 ± 0.03 ppb Re and total Os contents of 61.7 ± 0.2 to 90.2 ± 0.3 ppt (Table 4). The $^{187}Re/^{188}Os$ and $^{187}Os/^{188}Os$ ratios range from 512.0 ± 3.3 to 734.5 ± 4.9 and from 3.284 ± 0.026 to 4.624 ± 0.036, respectively. The Re-Os data together with the error correlation (*rho*) yield an *IsoplotR* (Vermeesch, 2018) Model 3 Re-Os isochron date of 358.3 ± 18.5 [18.6 including decay constant] Ma (2σ, Fig. 8a). The required variation by the regression of the Re-Os data in the initial $^{187}Os/^{188}Os$ composition is small (0.01 to

0.06). Using the initial $^{187}Os/^{188}Os$ composition given from the Re-Os isochron (0.22 ± 0.20), between 93.3% and 95.2% of the ^{187}Os in the pyrite is radiogenic ($^{187}Os^{r}$). Individual ^{187}Re-^{187}Os model ages are between 354.3 ± 34.1 and 360.5 ± 35.6 Ma, with a weighted average of 357.5 ± 9.0 Ma (2σ, MSWD = 0.02, Fig. 8b), which is within uncertainty of the Re-Os isochron date.

Eight marcasite samples yield highly variable Re (0.85 ± 0.01 to 64.14 ± 0.22 ppb) and total Os (7.9 ± 1.9 to 1429.9 ± 3.3 ppt) abundances (Table 4). The $^{187}Re/^{188}Os$ (112.3 ± 2.4 to 14233.5 ± 237.3) and $^{187}Os/^{188}Os$ (1.383 ± 0.04 to 110.56 ± 1.87) are variable, and yield no meaningful geological date.

Thermal history modelling

Thermal history based on Helium diffusion models was modeled using the HeFTy v.1.9 program (Ketcham, 2005). The objective of the modeling was to constrain time-temperature (t-T) paths that can reproduce measured zircon and apatite (U-Th)/He data. Only sample AX-39 was modeled given the best reproducibility of both zircon and apatite (U–Th)/He data. The model was parameterized as follows: diffusion kinetic parameters for zircon and apatite (U–Th)/He systems were adopted from Reiners et al. (2004) and Farley (2000), respectively; radii of the spherical diffusion domains were based on the measured size of the analyzed crystals and calculated equivalent sphere size; measured single grain ZHe and AHe ages that were closest to the population mean age were modelled as representative for the sample. A Monte-Carlo search method was applied to find 100 'good' thermal trajectories (goodness-of-fit (GOF) of >0.5) that could reconcile the pre-defined parameters and constraints. The starting point of the t-T path was set to T = 940°C at ~350–370 Ma based on zircon U-Pb data. The eruption of the volcanic rock was set at ~342 Ma according to the minimum zircon U-Pb ages of the rocks. The angular unconformity formed prior to the deposition of the Aqialehe Formation at 331 Ma suggests that the orebody was at near-surface conditions prior to 331 Ma and then buried by sediments. Accordingly, we set a constraint to T = 20–50°C at 331–342 Ma to reflect the near-surface residence prior to the burial, and another wide-open constraint was set to T = 50–250°C at 320–100 Ma (i.e., temperature range well above the closure temperature of zircon (U-Th)/He system) to estimate plausible maximum burial temperatures. The end of the t-T path was set to 10°C based on the average annual surface temperature in the area.

Thermal history modelling for sample AX-39 (Fig. 9) suggests that maximum temperatures of 120–180°C could be reached between ca. 250 and 160 Ma. Following the thermal maximum, the sample cooled to near-surface conditions (<50°C) no later than at 160 Ma and resided there until present day.

Interpretation and discussion

Here we first evaluate the morphological, chronological and geochemical data of zircon to demonstrate a long-lived magma system produced by periodic recharge. Then we discuss the temporal framework of volcanism and gold mineralization, and also document the role of reheating on the zircon and apatite (U-Th)/He systematics when coupled with regional geological constraints. We conclude by considering the geological significance of the newly recognized magma replenishment for gold mineralization, and the role of post-mineralization events for the preservation of the Paleozoic epithermal gold mineralization.

The andesitic host: Timeframe and magma recharge

Evidences of magma recharge

Zircon geochemistry is considered to primarily reflect the melt composition at the time of zircon crystallization (Claiborne et al., 2010), although zircon/melt partition coefficients are also sensitive to thermal and kinetic effects (Hoskin and Schaltegger, 2003). In this study, zircon compositional, textural, and CL features provide a time-correlated record of the evolving growth environment and offers significant value in distinguishing two zircon populations. The first population (Zr1) possesses low length-width ratios and exhibits wide growth bands (also called "widely spaced oscillatory zonation" by Vavra (1994) or patched zonation indicative of a low degree of zircon-saturation in the melt (Hoskin and Schaltegger, 2003). Calculated crystallization temperatures for Zr1 are relatively high (808 ± 36 °C), with the low Hf, U and Th concentrations and $(Yb/Gd)_N$ ratio suggesting low degree of fractionation (Claiborne et al., 2010). In contrast, the small (mostly 50 – 150 μm), often acicular crystals of Zr2 may have formed due to local saturation at the edge of an early-crystallizing phase (Bacon and Lowenstern, 2005). Its narrow-spaced oscillatory zoning represents kinetic effects at the crystal-melt interface, dependent on ordering in the melt by polymerization and often promoting local supersaturation and disequilibrium (Vavra, 1994; Hoskin and Schaltegger, 2003). The higher concentrations of Hf, U and Th, higher $(Yb/Gd)_N$ ratios, but lower Ti-in-zircon temperature in comparison with Zr1 suggests lower formation temperature (756 ± 21 °C) but higher degree of fractionation.

Interestingly, in the pyroxene andesite and quartz andesite, these two kinds of zircons, which could not have co-precipitated, coexist at hand sample-scale and even display overlapping $^{206}Pb/^{238}U$ ages within analytical uncertainty. In this case, the juxtaposition of crystals could provide evidence for mixing. Alternatively, these two kinds of zircon could also make up a more complexed zonation pattern, as exemplified by the embayed Zr1 core followed by later Zr2 overgrowths. The ubiquitous resorption surface and embayment (as shown by the narrow dark zone in Fig. 4b) in Zr1 suggest that the magma from which Zr1 crystallized was rejuvenated or mixed with hotter and/or zircon-undersaturated pulses of magma, and then quenched with the cooler felsic melt recorded by Zr2. Due to the limited thickness, no geochronological or geochemical data can be obtained for the dark zone, but the age of magma recharge could be roughly bracketed between crystallization ages of Zr1 and Zr2, i.e., 351–357 Ma and 340 Ma. Occasionally, the high temperature Zr1 is surrounded by cooler Zr2 without this intermediate dark zone, which could have resulted from buffering of zircons as inclusions in phenocrysts during periods of rejuvenation and dissolution (Miller et al., 2007).

In the amphibole andesite and andesite where only Zr1 is present, monotonic cooling and progressive fractionation is not favored. According to Siégel et al. (2018), monotonic cooling and progressive fractionation would induce a continuous increase of Hf, U abundances, and a concomitant decrease of Ti-in-zircon temperature and Th/U would be expected. This is certainly not the case of our sample (Fig. S1). In contrast, systems dominated by magmatic recharge would have mixed or mingled glasses, and minerals with disequilibrium textures from rapid pre-eruptive growth or dissolution (Streck et al., 2007). Such a conclusion is further supported by the complex zonation of plagioclase phenocrysts (inverse zoning, patchy zoning and crystal dissolution-reprecipitation, sieve and spongy textures) from the same samples as dated in this paper (Zhang, 2020).

Time frame of magmatism

Repeated magma recharge extensively mixes materials from spatially disparate portions of the magma chamber, so that minerals in a single hand-sample may be largely unrelated to each other or to their host liquid (matrix glasses). Zircons from our andesitic samples show a large time span between 377 and 338 Ma (Fig. 6), this is in keeping with the scenario of repeated magma injection into a fairly dynamic, mushy magma chamber, but makes the interpretation of zircon U-Pb age inherently difficult.

To identify principal age populations, we used the method of Sambridge and Compston (1995). As shown in Figure 6, the older zircons constitute a peak at around 361 Ma for the pyroxene andesite (360.9 ± 2.1 Ma) and amphibole andesite (361.9 ± 1.8 Ma), and a peak at around 355 Ma for the quartz andesite (355.3 ± 1.7 Ma) and andesite (354.3 ± 2.4 Ma). These zircons are interpreted as antecrysts crystallized from an earlier magma pulse and were incorporated into a later one (Bacon and Lowenstern, 2005; Miller et al., 2007). The youngest zircon analyses from the four samples yield overlapping $^{206}Pb/^{238}U$ ages around 342 Ma (Fig. 6a-d). They are interpreted as autocrystic zircon growth in the last magma increment. The weighted mean average age of 341.5 ± 2.0 Ma (n = 15, MSWD = 0.46, Fig. 6f) would thus be the closest approximation to the last emplacement age. This age is consistent with the previously obtained whole rock Rb-Sr isochron age of 345.9 ± 9 Ma (Li et al., 1998) within uncertainty (Table 1).

There are zircons yielding much older $^{206}Pb/^{238}U$ ages between 368 and 380 Ma. These data fall into the age range reported for the earlier volcanic member of the Dahalajunshan Formation (362 – 417 Ma; An et al., 2013; Yu et al., 2016, 2018; Ye et al., 2020), and are also interpreted as antecrysts. Two old outliers aged at 1693 ± 22 Ma ($^{207}Pb/^{206}Pb$ age) and 435.8 ± 2.8 Ma ($^{206}Pb/^{238}U$ age) come from zircon cores surrounded by Zr1 and represent zircon xenocrysts that are unrelated to the magma systems.

Timing of gold mineralization

Previous studies aimed to constrain the gold mineralization age by Rb-Sr or Ar/Ar dating of hydrothermal sericite or fluid inclusions (Table 1). The recent development of the Re-Os geochronometer provides a viable alternative by directly dating sulfide minerals (Stein et al., 2000; Selby et al., 2009). The use of Re-Os pyrite geochronology is particularly useful at Axi, not only because pyrite is ubiquitous, and displays variable textural features and deposit-wide crosscutting relationships, but also it hosts appreciable concentrations of invisible gold and thus is a direct witness of the ore-forming process (Zhang et al., 2018; Li et al., 2023).

The coarse-grained, auriferous pyrites used for Re-Os dating pre-date the tiny, oscillatory zoned pyrite (Zhang et al., 2018; Liu et al., 2020; Li et al., 2023). Our Re-Os dating of four coarse-grained pyrite separates yielded an isochron age of 358.3 ± 18.5 [18.6] Ma, which is identical to the Re-Os age of 353 ± 6 Ma obtained by Liu et al. (2020). Despite the large uncertainty, these data strongly support pyrite formation and gold mineralization at ca. 355 Ma. Such an age is older than the latest eruption of the andesite host (341.5 ± 2.0 Ma), but overlaps with the age of the mineralized monzonite porphyry enclaves (356.2 ± 4.3 Ma, zircon U-Pb age, Zhao et al., 2014b) at nearby Tawuerbieke gold deposit (~2 km south of Axi). Also, at the Tawuerbieke deposit, there is a granitic porphyry aged 355–349 Ma (zircon U-Pb age, Tang et al., 2013; Zhao et al., 2014a) that is considered to be the progenitor to gold mineralization (Zhao et al., 2014a). These geological and geochronological features favor a potential link to porphyry mineralization that may be a precursor to epithermal mineralization.

At Axi, marcasites are prevalent and closely associated with the calcite and quartz/chalcedony. Paragenetically, the marcasites post-date the fine-grained, oscillatory zoned pyrite (Li et al., 2023). Although no meaningful isochron age is obtained for our marcasite samples, the work of Liu et al.

(2020) reported a Re-Os isochron age of 332 ± 8 Ma for the fine-grained pyrite, about 20 Myrs younger than the coarse-grained auriferous pyrite. This Re-Os pyrite age is interpreted to date the second pulse of gold (epithermal) mineralization. The maximum termination of gold mineralization is well constrained by the pronounced angular unconformity between the overlying Carboniferous (Visean)-aged Aqialehe Formation and the basal conglomerate/placer-style gold orebody (Zhai et al., 2009). Such a robust geological relationship precludes a Permian gold mineralization event (An and Zhu, 2018; Dong et al., 2018), but instead, suggests that gold mineralization and the andesite host were once exposed to erosion no later than 331 Ma (minimum age for the Visean as suggested by the International Commission on Stratigraphy, 2020). Moreover, given that the younger phase of gold (epithermal) mineralization is nominally only 1 Myr older than the overlying Aqialehe Formation, it suggests that exhumation of the Axi deposit and surrounding region was rapid (see below discussion).

The post-eruption thermal history

In this study, the andesitic rocks from the footwall of F2 were selected for combined zircon U-Pb, ZHe and AHe analysis. They are separated from the gold orebodies by F2, and their post-eruption thermal history can be applied to the Axi deposit.

The latest eruption age of the andesitic rocks was constrained to 341.5 ± 2.0 Ma by our new zircon U-Pb data. Such a result is consistent with the fact that they were unconformably covered by the Visean-aged Aqialehe Formation, but much older than the ZHe age of 317.9 ± 9.8 Ma. Interestingly, a similar K-feldspar $^{40}Ar/^{39}Ar$ plateau age of 313.5 ± 2.2 Ma is reported for the mineralized monzonite porphyry enclave hosted by andesite at the nearby Tawuerbieke deposit (Zhao et al., 2021). This implies significant post-eruption reheating events. Sedimentary burial would induce temperature increase and hence potentially influence the zircon (U-Th)/He systematics (Fox and Shuster, 2014). The thickness of the Aqialehe Formation (~2 km; Li et al., 2018), however, is not stratigraphically thick enough to fully reset the (U-Th)/He system in zircon. The epithermal mineralization at 332 Ma may be a potential contributor, although there is limited or no hydrothermal alteration for the studied andesitic rocks. Alternatively, we speculate that the ZHe age might reflect an emplacement of a younger intrusion as seen in the nearby Tawuerbieke gold deposit (315.2 ± 3.5 Ma; Peng et al., 2016). This tentative interpretation, however, needs to be corroborated by additional data obtained by future investigations.

Burial induced temperature increase would also influence the AHe system giving its very low closure temperature. Therefore, obtained ZHe and AHe cannot represent the age of volcanic eruption, but instead, record the passage of the sample through their helium partial retention zone (HePRZ) (Reiners and Brandon, 2006). Our thermal history modelling results suggest maximum temperatures of ~120-180 °C for the Mesozoic era, which corresponds to burial depth of at least 4.4 km during 318−149 Ma (age bracketed by ZHe and AHe) assuming a paleo-geothermal gradient of 25 °C/km. This result is consistent with previous calculation of Wang et al. (2018), who proposed a stratigraphic cover of ~4.8 km overlying the Dahalajunshan Formation.

The exhumation rate between 149 Ma and 120 Ma can be calculated using age-elevation relationship (Fig. 7). Although covering a limited vertical distance of 300 meters and acknowledging the scatter of the AHe dates, we argue that there is a well-preserved AHe variation with elevation that resembles theoretical He retention vs. depth curves (Wolf et al., 1998) and age-elevation relationship obtained for other He vertical-profile studies (Reiners and Brandon, 2006). Assuming: (1) the closure isotherm was flat at the time of closure, (2) at a given time, erosion rates were the same for all of the samples, and (3) the depth of the closure isotherm has remained constant (Reiners and Brandon, 2006), regression through the central AHe ages suggests an exhumation rate of 9.8 m/Ma between 149 and 120 Ma (R^2=0.79).

Preservation potential of epithermal deposits in the Tulasu basin

Paleozoic epithermal deposits are relatively less common than their Mesozoic or Cenozoic counterparts due to their high susceptibility to tectonic uplift and erosion in rapidly uplifting arcs above subduction zones (Richards, 2009). The post-mineralization history is thus critical to their preservation potential (Kesler et al., 2004; Groves et al., 2005). Combined stratigraphic relationships and chronological data constrain a complex geological history for the Axi deposit, where the slightly eroded epithermal mineralization was unconformably covered by thick sediments of the Aqialehe Formation in ~1 Myrs following the last gold (epithermal) mineralization event. Such post-mineralization stratigraphic events favor preservation of old epithermal deposits, as suggested for the epithermal Au-Ag systems in the Camaguey District, Cuba, the Pueblo Viejo deposit in the Dominican Republic, the Pajingo deposit in Queensland, the Cerro Vanguardia auriferous system in Argentina, and the Mallery Lake deposit in Canada (Turner et al., 2001; Kesler et al., 2004).

Viewed in this context, the Tulasu Basin is an excellent target for preserved epithermal mineralization. However, the currently-known epithermal(-porphyry) gold deposits are restricted to the central and northern part of the basin, with the southern section of the basin lacking important epithermal mineralization (Fig. 2). Recently, Wang et al. (2021) and Zhao et al. (2021) utilized detailed apatite fission track analysis as well as geological mapping, in an attempt to reveal the thermal history of the Tulasu Basin. Combined with our new data, the result indicates heterogeneous exhumation where the southern part was exhumed significantly in comparison with the northern part of the basin. This is verified by the exposure of coarse-grained batholitic rocks in the southern part of the basin (Fig. 2). Actually, most volcanic arcs that host epithermal mineralization lack widespread exposure of coeval plutonic rocks; even if there are indeed some intrusive rocks, they are small stocks or plugs rather than batholiths (Richards and Kerrich, 1993). According to White and Hedenquist (1990), favorability for epithermal mineralization would decrease with increasing exposure of coarse-grained batholitic rocks.

Tectonic evolution of the Chinese Western Tianshan

The presented dataset (Table 1) is the first combing both high- and low-temperature geo-/thermochronological constraints for the studied Axi deposit. The data not only provide a full record of deposit formation and exhumation (Fig. 10), but also shed light on the tectonic evolution of the Yili Block and the Chinese Western Tianshan.

The tectonic setting of Devonian to Carboniferous volcanic rocks along the northern margin of the Yili Block is hotly debated. Che et al. (1994) proposed that they formed in a continental rift, whereas Xia et al. (2004) attributed them to products of a mantle plume. Yet, other researchers (e.g., An et al., 2013; Xiao et al., 2013; Yu et al., 2016, 2018) suggest a continetal arc setting. Our study reveals that the andesitic host to the Axi deposit was constructed by incremental addition of small magma batches, with pulses of zircon crystallization at 362, 354 and 342 Ma. The andesitic geochemical (enrichment of LILE and LREE, depletion of HFSE and HREE) and isotopic data (zircon $\varepsilon Hf(t) = 0.5$ to 9.2, whole-rock $\varepsilon Nd(t) = -0.94$ to 1.78) reveal an arc magma affinity (Zhang, 2020), consistent with other volcano-sedimentary rocks from the Dahalajunshan Formation aged 310–417 Ma (Yu et al., 2018 and references therein). The $^{206}Pb/^{207}Pb$ age of one zircon core (1693 ± 22 Ma) falls into the age range (1620 – 1720 Ma) reported for inherited zircons from one trachyandesite sample collected from Laerdundaban to the east. The age of the inherited zircons, coupled with the development of Neoproterozoic meta-sedimentary rocks (Wenquan Group), support the presence of a Precambrian basement (Zhu et al., 2009; Li et al., 2013; Huang et al., 2016). The earlier ca. 355 Ma gold mineralization is attributed to a potential link with porphyry-style mineralization (Zhao et al., 2014b; Liu et al., 2020), and the later ca. 332 Ma epithermal gold mineralization cemented the earlier mineralized clasts. Thus, the volcanic (An et al., 2013; Yu et al., 2016, 2018), plutonic (Zhao et al., 2014b; Liu et al., 2020) as well as epithermal-porphyry gold mineralization events (Peng et al., 2018; Zhang et al., 2018; Ye et al. 2020) confirm an Andean-type magmatic arc built on the margin of a Precambrian microcontinent (Wang et al., 2009; Zhu et al., 2009; Xiao et al., 2013; Yu et al., 2016, 2018; Zhang, 2020). Post-mineralization of the Axi deposit (~ 1 – 9 Myr when taking the uncertainty into consideration), the orebody and andesite host were exhumed to surface, slightly eroded (by ~360 m according to Zhai et al. 2009), and then concealed by the Aqialehe Formation no later than 331 Ma. The exhumation was linked to the southward subduction of the North Tianshan Ocean (Wang et al., 2006; Tang et al., 2013; An et al., 2013), or to northward, flat-slab subduction of the South Tianshan Ocean (Gao et al., 2009; Zhu et al., 2009; Han et al., 2011; Tan et al., 2022). Subsequent slab roll-back of the South Tianshan Ocean (Tan et al., 2022) possibly resulted in local extension and deposition of the Aqialehe Formation. The sedimentary burial and potential intrusion (either in the nearby Tawuerbieke area or blind intrusions at Axi) provided sufficient heat to sustain around 180°C until 318 Ma. The post-mineralization thermal event seems to have had no significant effect on gold mineralization, given indicative epithermal textures such as open space-filling, lattice texture of calcite/quartz, and crustiform banding are still well preserved (Zhai et al., 2009; Liu et al., 2020).

Previous thermochronological data reveal important Late Paleozoic cooling found in the main mountains in the Western Tianshan (Dumitru et al., 2001; Jolivet et al., 2001). It coincides with, or slightly earlier than the intrusion of post-collision granitic and alkaline units (Glorie et al., 2010; Yu et al., 2018), the development of strike-slip faults along the Main Tianshan Shear zone (Shu et al., 1999), indicating an important tectonic event and may also be responsible for the unconformity between the Permian and older rocks (Feng et al., 2000). This event is attributed to the closure of the South Tianshan Ocean and subsequent collision between the Tarim and Yili-Central Tianshan plates (Li et al., 2020; Jia et al., 2022; Sun et al., 2023), although the final closure and associated collision may be heterogenous, since the sandstone within a fore-arc accretionary basin close to the Akeyazi low temperature ultra-high pressure metamorphic complex could be dated back to Triassic (Tan et al., 2022). The uplift and erosion of the surrounding mountain belt, especially the Keguqinshan to the north (Fig. 1c), provided sufficient sediments for the Tulasu Basin (Wang et al., 2018). Our thermochronological data further constrain the thickness of sediments to 4.4 km between 318 – 149 Ma, which serves as an important concealment for the epithermal deposits.

The geographic situation west of the bulwark of Tibet and north of the Pamir enabled maximum impact of the tectonics of the India-Asia collision (Xiao et al., 2013). The Late Mesozoic cooling in the whole Tianshan region is considered to reflect structural reactivation of the Tianshan through the collision of the Lhasa block with the southern margin of Asia during the latest Jurassic-earliest Cretaceous (Dumitru et al., 2001; Jolivet et al., 2001; Wang et al., 2018; Gong et al., 2021). It is consistent with the stratigraphic record where the deformed Jurassic strata are cut by reverse faults and underlain by undeformed Upper Cretaceous strata (Feng et al., 2000). The absence of Late Jurassic-Early Cretaceous sedimentation may be also a response to the exhumation. As demonstrated by our apatite (U-Th)/He data, Late Jurassic-Early Cretaceous exhumation for the Tulasu Basin was very slow, at a rate of 9.8 m/Ma.

Conclusions

A multi-system geo-/thermochronometry approach including zircon U-Pb, zircon (U-Th)/He, apatite (U-Th)/He and pyrite Re-Os dating reveals the thermal history of the Paleozoic Axi epithermal system and the tectonics of the Chinese Western Tianshan where it is located. The andesitic host to the Axi deposit is a prime example of a long-lived, large-volume magma system that was produced by periodic recharge of the magma chamber. The youngest zircon group records the latest volcanic eruption at 342 Ma. The gold mineralization occurred at 355 Ma and 332 Ma, with the former attributed to precursor porphyry mineralization and the latter to epithermal mineralization. The thermal collapse most likely occurred after 318 Ma and was facilitated by rapid denudation and subsequent burial and intrusion. The post-mineralization deposition and Late Mesozoic (149 – 121 Ma) erosion of sedimentary cover protected the shallow mineralization from erosion. Our work confirms that the Chinese Western Tianshan was an Andean-type Paleozoic magmatic arc and experienced local transition from compression to extension around 331 Ma, Late Paleozoic uplift of the Keguqinshan Mountain leading to the formation of the Tulasu Basin, and finally Late Mesozoic tectonic exhumation of the whole region.

Acknowledgments

The Geological Team 703 of the Xinjiang Bureau of Nonferrous Metals, the Western Gold Co., Ltd, Jie Yu, Yanshuang Wu, and Xi Chen are kindly acknowledged for help during field work. We thank Antonia Hofmann, Chris Ottley and Geoff Nowell for their analytical support. MD was supported by the AuScope NCRIS2 program and Curtin Research Fellowship. MD acknowledges the help of Adam Frew and Bryant Ware with mineral dissolution and solution ICP-MS analyses, and thanks István Dunkl for sharing PepiFLEX software for ICP-MS data reduction. Yildirim Dilek, Kathryn Cutts, Gilby Jepson and an anonymous reviewer are thanked for their insightful comments.

Funding

The research was financially supported by the Xinjiang Outstanding Youth Scientific Grant (No. 2020Q006), the National Natural Science Foundation of China (No. 42122014, 41888101), and the Xinjiang Key Research Project (No.2021A03001-2). This is a contribution to IGCP 662 and IGCP 669.

Statements and declarations

The authors declare that the research was conducted in the absence of any commercial or financial relationships that could be construed as a potential conflict of interest.

References

An, F., and Zhu, Y.F. 2018. Geology and geochemistry of the Early Permian Axi low-sulfidation epithermal gold deposit in North Tianshan (NW China). Ore Geology Reviews 100, 12–30, https://doi.org/10.1016/j.oregeorev.2017.03.021

An, F., Zhu, Y.F., Wei, S., and Lai, S.C. 2013. An Early Devonian to Early Carboniferous volcanic arc in North Tianshan, NW China: Geochronological and geochemical evidence from volcanic rocks. Journal of Asian Earth Sciences, 78, 100–113, https://doi.org/10.1016/j.jseaes2013.07.037

Bacon, C.R., and Lowenstern, J.B. 2005. Late Pleistocene granodiorite source for recycled zircon and phenocrysts in rhyodacite lava at Crater Lake, Oregon. Earth and Planetary Science Letters, 233, 277–293, https://doi.org/10.1016/j.epsl.2005.02.012

Che, Z.C., Liu, H.F., and Liu, L. (eds) 1994. Formation and evolution of the Middle Tianshan Orogenic Belt. Geological Publishing House, Beijing (in Chinese)

Chen, Y.J., Pirajno, F., Wu, G., Qi, J.P., and Xiong, X.L. 2012. Epithermal deposits in North Xinjiang, NW China. International Journal of Earth Sciences, 101, 889–917, https://doi.org/10.1007/s00531-011-0689-4

Claiborne, L.L., Miller, C.F., and Wooden, J. 2010. Trace element composition of igneous zircon: a thermal and compositional record of the accumulation and evolution of a large silicic batholith, Spirit Mountain, Nevada. Contributions to Mineralogy and Petrology, 160, 511–531, https://doi.org/10.1007/s00410-010-0491-5

Cooke, D., and Simmons, S. 2000. Characteristics and genesis of epithermal gold deposit. Reviews in Economic Geology, 13, 221–244.

Creaser, R.A., Papanastassiou, D.A., and Wasserburg, G..J., 1991, Negative thermal ion mass spectrometry of osmium, rhenium and iridium. Geochimica et Cosmochimica et Acta, 55, 397–401.

Danišík, M., Pfaff, K., Evans, N. J., Manoloukos, C., Staude, S., McDonald, B. J., and Markl, G., 2010, Tectonothermal history of the Schwarzwald Ore District (Germany): An apatite triple dating approach. Chemical Geology, 278, 58–69, https://doi.org/10.1016/j.chemgeo.2010.08.022.

Danišík, M., Shane, P., Schmitt, A.K., Hogg, A., Santos, G.M., Storm, S., Evans, N.J., Fifield, L.K., and Lindsay, J.M. 2012. Re-anchoring the late Pleistocene tephrochronology of New Zealand based on concordant radiocarbon ages and combined 238U/230Th disequilibrium and (U–Th)/He zircon ages. Earth and Planetary Science Letters, 349, 240–250, https://doi.org/10.1016/j.epsl.2012.06.041

Danišík, M., McInnes, B. I., Kirkland, C. L., McDonald, B. J., Evans, N. J., and Becker, T. 2017. Seeing is believing: Visualization of He distribution in zircon and implications for thermal history reconstruction on single crystals. Science Advances, 3, e1601121, https://doi.org/10.1126/sciadv.1601121

Dong, L.H., and Sha, D.M. (eds) 2005. Late paleozoic epithermal gold deposits in West Tianshan. Geological Publishing House, Beijing (in Chinese).

Dong, L.L, Wan, B., Deng, C., Cai, K.D., and Xiao, W.J. 2018. An Early Permian epithermal gold system in the Tulasu Basin in North Xinjiang, NW China: constraints from in situ oxygen-sulfur isotopes and geochronology. Journal of Asian Earth Sciences, 153, 412–424, https://doi.org/10.1016/j.jseaes.2017.07.044

Dumitru, T.A., Zhou, D., Chang, E.Z., Graham, S.A., Hendrix, M.S., Sobel, E.R. and Carroll, A.R. 2001. Uplift, exhumation, and deformation in the Chinese Tian Shan. Geological Society of America Memoir, 71–99.

Evans, N. J., Byrne, J. P., Keegan, J. T., and Dotter, L. E., 2005: Determination of uranium and thorium in zircon, apatite, and fluorite: application to laser (U–Th)/He thermochronology.

Journal of Analytical Chemistry, 60(12), 1159-1165.

Farley, K.A., Wolf, R.A., and Silver, L.T., 1996: The effects of long alpha-stopping distances on (U-Th)/He ages. Geochimica et Cosmochimica Acta, 60, 4223-4229.

Farley, K. 2000. Helium diffusion from apatite: General behavior as illustrated by Durango fluorapatite. Journal of Geophysical Research-Solid Earth, 105, 2903–2914, https://doi.org/10.1029/1999JB900348

Feng, J.H., Jiang, Z.X., Lu, H.B., He, H.S., Ma, W.M., and Chen, F.L.(eds) 2000. The Reaserch on Sequence Stratigraphy and Sedimentology in Ili Basin. Petroleum University Press, Dongying (in Chinese).

Ferry, J., and Watson, E. 2007. New thermodynamic models and revised calibrations for the Ti-in-zircon and Zr-in-rutile thermometers. Contributions to Mineralogy and Petrology, 154, 429–437, https://doi.org/10.1007/s00410-007-0201-0

Flowers, R.M., Ketcham, R.A., Shuster, D.L. and Farley, K.A., 2009. Apatite (U–Th)/He thermochronometry using a radiation damage accumulation and annealing model. Geochimica et Cosmochimica acta, 73, 2347-2365.

Fox, M., and Shuster, D.L. 2014. The influence of burial heating on the (U–Th)/He system in apatite: Grand Canyon case study. Earth and Planetary Science Letters, 397, 174–183, https://doi.org/10.1016/j.epsl.2014.04.041

Gao, J., Long, L., Klemd, R., Qian, Q., Liu, D., Xiong, X., Su, W., Liu, W., Wang, Y., and Yang, F. 2009. Tectonic evolution of the South Tianshan orogen and adjacent regions, NW China: geochemical and age constraints of granitoid rocks. International Journal of Earth Sciences, 98, 1221–1238, https://doi.org/10.1007/s00531-008-0370-8

Glorie, S., De Grave, J., Buslov, M., Elburg, M., Stockli, D., and Gerdes, A.J. 2010. Multi-method chronometric constraints on the evolution of the Northern Kyrgyz Tien Shan granitoids (Central Asian Orogenic Belt): from emplacement to exhumation. Journal of Asian Earth Sciences, 38, 131–146, https://doi.org/10.1016/j.jseaes.2009.12.009

Gong, L,, Kohn, B.P., Zhang, Z.Y., Xiao, B., Wu, L., and Chen, H.Y. 2021. Exhumation and Preservation of Paleozoic Porphyry Cu Deposits: Insights from the Yandong Deposit, Southern Central Asian Orogenic Belt. Economic Geology, 116, 607–627, https://doi.org/10.5382/econgeo.4812

Groves, D.I., Condie, K.C., Goldfarb, R.J., Hronsky, J.M.A., and Vielreicher, R.M. 2005. Secular changes in global tectonic processes and their influence on the temporal distribution of gold-bearing mineral deposits. Economic Geology, 100, 203–224, https://doi.org/10.2113/100.2.203

Han, B.F., He, G.Q., Wang, X.C., and Guo, Z.J., 2011. Late Carboniferous collision between the Tarim and Kazakhstan–Yili terranes in the western segment of the South Tian Shan Orogen, Central Asia, and implications for the North Xinjiang, western China. Earth-Science Reviews 109, 74–93, https://doi.org/10.1016/j.earscirev.2011.09.001.

Hoskin, P.W.O., and Schaltegger, U. 2003. The composition of zircon and igneous and metamorphic petrogenesis. Reviews in Mineralogy & Geochemistry, 53, 27–62, https://doi.org/10.2113/0530027

Hourigan, J.K., Reiners, P.W. and Brandon, M.T., 2005. U-Th zonation-dependent alpha-ejection in (U-Th)/He chronometry. Geochimica et Cosmochimica Acta, 69, 3349-3365.

Huang, Z., Long, X., Yuan, C., Sun, M., Wang, Y., Zhang, Y., Chen, B., 2016. Detrital zircons from Neoproterozoic sedimentary rocks in the Yili Block: Constraints on the affinity of microcontinents in the southern Central Asian Orogenic Belt. Gondwana Research, 37, 39-52 , https://doi.org/10.1016/j.gr.2016.05.009

Jiang, T., Gao, J., Klemd, R., Qian, Q., Zhang, X., Xiong, X., Wang, X., Tan, Z., and Chen, B., 2014. Paleozoic ophiolitic melanges from the South Tianshan Orogen, NW China: Geological, geochemical and geochronological implications for the geodynamic setting. Tectonophysics, 612, 106-127, https://doi.org/10.1016/j.tecto.2013.11.038

Jolivet, M., Brunel, M., Seward, D., Xu, Z., Yang, J., Roger, F., Tapponnier, P., Malavieille, J., Arnaud, N., and Wu, C. 2001. Mesozoic and Cenozoic tectonics of the northern edge of the Tibetan plateau: fission-track constraints. Tectonophysics, 343, 111–134, https://doi.org/10.1016/S0040-1951(01)00196-2

Ketcham, R.A. 2005. Forward and Inverse Modeling of Low-Temperature Thermochronometry Data. Reviews in Mineralogy & Geochemistry, 58, 275–314, https://doi.org/10.2138/rmg.2005.58.11

Kesler, S. E. and Wilkinson, B. H. 2006. The role of exhumation in the temporal distribution of ore deposits. Economic Geology, 101, 919-922, https://doi.org/10.2113/gsecongeo.101.5.919

Kesler, S.E., Hall, C.M., Russell, N., Pinero, E., Sanchez, R.C., Perez, M.R., and Moreira, J. 2004. Age of the Camaguey gold-silver district, Cuba: Tectonic evolution and preservation of epithermal mineralization in volcanic arcs. Economic Geology, 99, 869–886

Kröner, A., Alexeiev, D., Rojas-Agramonte, Y., Hegner, E., Wong, J., Xia, X., Belousova, E., Mikolaichuk, A., Seltmann, R., and Liu, D. 2013. Mesoproterozoic (Grenville-age) terranes in the Kyrgyz North Tianshan: zircon ages and Nd–Hf isotopic constraints on the origin and evolution of basement blocks in the southern Central Asian Orogen. Gondwana Research, 23, 272–295, https://doi.org/10.1016/j.gr.2012.05.004

Li, H.Q, Xie, C.F., and Chang, H.L. 1998. Study on metallogenic chronology of nonferrous and precious metallic ore deposits in northern Xinjiang, China. Geological Publication House, Beijing (in Chinese with English abstract).

Li, K., Wang, B., Shu, L., Wang, F., Liu, H., 2013. Geological Features, Ages, and Tectonic Implications of the Wenquan Group in NW Chinese Tianshan. Geological Journal of China Universities, 19, 491-503 (in Chinese with English abstrct)

Li, N., Zhang, B., Ulrich, T., Williams-Jones, A.E., Chen, Y.J., 2023. Magmatic degassing controlled the metal budget of the Axi epithermal gold deposit. American Mineralogist, https://doi.org /10.2138/am-2022-8610

Li, P.F., Sun, M., Rosenbaum, G., Cai, K.D., Yuan, C., Jourdan, F., Xia, X.P., Jiang, Y.D., Zhang, Y.Y. 2020. Tectonic evolution of the Chinese Tianshan Orogen from subduction to arc-continent collision: Insight from polyphase deformation along the Gangou section, Central Asia. Geological Society of America Bulletin, https://doi.org /10.1130/B35353.1Li, Y., Xu, Q., Yang, G., Wang, R., Tong, L., Li, G., Shen, R., Li, Z., Wang, Z., and Wang, Z.J. 2018. Carboniferous tectonic configuration of the Yining Massif in Western Tianshan, NW China. Geological Journal, 53, 60–75, https://doi.org/10.1002/gj.3236

Liu, Z., Mao, X., Deng, H., Li, B., Zhang, S., Lai, J., Bayless, R. C., Pan, M., Li, L., and Shang, Q., 2018. Hydrothermal processes at the Axi epithermal Au deposit, western Tianshan: Insights from geochemical effects of alteration, mineralization and trace elements in pyrite. Ore Geology Reviews, 102, 368-385, https://doi.org/10.1016/j.oregeorev.2018.09.009

Liu, Z., Mao, X., Ackerman, L., Li, B., Dick, J.M., Yu, M., Peng, J., and Shahzad, S.M. 2020. Two-stage gold mineralization of the Axi epithermal Au deposit, Western Tianshan, NW China: Evidence from Re–Os dating, S isotope, and trace elements of pyrite. Mineralium Deposita, 55, 863−880, https://doi.org/10.1007/s00126-019-00903-6

McDowell, F.W., McIntosh, W.C., and Farley, K. A. 2005. A precise ^{40}Ar–^{39}Ar reference age for the Durango apatite (U–Th)/He and fission-track dating standard. Chemical Geology 214, 249-263.

Miller, J.S., Matzel, J.E., Miller, C.F., Burgess, S.D., and Miller, R.B. 2007. Zircon growth and recycling during the assembly of large, composite arc plutons. Journal of Volcanology and Geothermal Research, 167, 282–299, https://doi.org/10.1016/j.jvolgeores.2007.04.019

Peng, Y.W., Gu, X.X., Cheng, W.B., Zou, C.H., Mi, D.J., and Niu, C.L. 2016. Genesis of the Tawuerbieke gold deposit in the Tulasu basin, western Tianshan: Evidence from geochronology and stable isotopes. Acta Petrologica Sinica, 32, 1361−1378 (in Chinese with English abstract).

Peng, Y.W., Gu, X.X., Cheng, W.B., Zhao, X.B., Wang, G.N., Lu, L.T., and Han, J.M. 2018. Metallogenesis of the Late Palaezoic Axi-Tawuerbieke Au-Pb-Zn district in the Tulasu Basin, Western Tianshan, China: Constraints from geological characteristics and isotope geochemistry. Geological Journal, 53, 3030–3050, https://doi.org/10.1002/gj.3141

Reiners, P. W., 2005, Zircon (U-Th)/He thermochronometry. In Reiners, P. W., and Ehlers, T. A., (eds.) Low-Temperature Thermochronology: Techniques, Interpretations, and Applications, 58, 151-179, https://doi.org/10.2138/rmg.2005.58.6

Reiners, P.W., and Brandon, M.T. 2006. Using thermochronology to understand orogenic erosion. Annual Review of Earth and Planetary Sciences, 34, 419–466, https://doi.org/10.1146/annurev.earth.34.031405.125202

Reiners, P.W., Spell, T.L., Nicolescu, S., and Zanetti, K.A. 2004. Zircon (U-Th-[Sm])/He thermochronometry: He diffusion and comparisons with 40Ar/39Ar dating. Geochimica et Cosmochimica Acta, 68, 1857−1887, https://doi.org/10.1016/j.gca.2003.10.021

Richard, J.P. 2009. Postsubduction porphyry Cu-Au and epithermal Au deposits: Products of remelting of subduction-modified lithosphere. Geology, 37, 247–250, https://doi.org/10.1130/G25451A.1

Richards, J.P., and Kerrich, R. 1993. The Porgera gold mine, Papua New Guinea; magmatic hydrothermal to epithermal evolution of an alkalic-type precious metal deposit. Economic Geology, 88, 1017−1052, https://doi.org/10.2113/gsecongeo.88.5.1017

Safonova, I., Biske, G., Romer, R. L., Seltmann, R., Simonov, V., and Maruyama, S., 2016. Middle Paleozoic mafic magmatism and ocean plate stratigraphy of the South Tianshan, Kyrgyzstan. Gondwana Research, 30, 236-256, https://doi.org/10.1016/j.gr.2015.03.006

Sambridge, M., and Compston, W. 1995. Mixture modeling of multi-component data sets with application to ion-probe zircon ages. Earth and Planetary Science Letters, 128, 373–390. https://doi.org/10.1016/0012-821X(94)90157-0

Selby, D., Kelley, K.D., Hitzman, M.W., and Zieg, J. 2009. Re-Os sulfide (bornite, chalcopyrite, and pyrite) systematics of the carbonate-hosted copper deposits at Ruby Creek, southern Brooks Range, Alaska. Economic Geology, 104, 437–444, https://doi.org/10.2113/gsecongeo.104.3.437

Shu, L., Charvet, J., Guo, L., Lu, H., and Laurent-Charvet, S. 1999. A large-scale Palaeozoic dextral ductile strike-slip zone: the Aqqikkudug–Weiya Zone along the Northern margin of the Central

Tianshan Belt, Xinjiang, NW China. Acta Geologica Sinica, 73, 148−162 (in Chinese with English abstract).

Shirey, S. B., and Walker, R. J., 1995, Carius tube digestion for low-blank rhenium-osmium analysis. Analytical Chemistry, 67, 2136-2141.

Shuster, D.L., Flowers, R.M. and Farley, K.A., 2006. The influence of natural radiation damage on helium diffusion kinetics in apatite. Earth and Planetary Science Letters, 249, 148-161.

Simmons, S.F., White, N.C., and John, D.A. 2005. Geological characteristics of epithermal precious and base metal deposits. Economic Geology, 29, 485−522

Siégel, C., Bryan, S., Allen, C., and Gust, D.A. 2018. Use and abuse of zircon-based thermometers: a critical review and a recommended approach to identify antecrystic zircons. Earth-Science Reviews, 176, 87−116, https://doi.org/10.1016/j.earscirev.2017.08.011

Smoliar, M.I., Walker, R.J., and W., M.J., 1996, Re-Os isotope constraints on the age of Group IIA, IIIA, IVA, and IVB iron meteorites. Science, 271, 1099–1102.

Spencer, C. J., Danisik, M., Ito, H., Hoiland, C., Tapster, S., Jeon, H., McDonald, B., and Evans, N. J., 201. Rapid Exhumation of Earth's Youngest Exposed Granites Driven by Subduction of an Oceanic Arc. Geophysical Research Letters, 46, 1259-1267, https://doi.org/10.1029/2018GL080579

Stein, H.J., Morgan, J.W., and Scherstén A. 2000. Re-Os dating of low-level highly radiogenic (LLHR) sulfides: The Harnas gold deposit, southwest Sweden, records continental-scale tectonic events. Economic Geology, 95, 1657-1671, https://doi.org/10.2113/95.8.1657

Streck, M.J., Leeman, W.P., and Chesley, J. 2007. High-magnesian andesite from Mount Shasta: A product of magma mixing and contamination, not a primitive mantle melt. Geology, 35, 351–354, https://doi.org/10.1130/G23286A.1

Sun, J.B., Qin, K.Z., Chen, W., Liu, Y.H., Shen, Z., Zhang, B., Zhang, Z.Y., Xing, L., Zhao, S.F., Zhang, W., Yin, J.Y., 2023. Exhumation history of the Katebasu gold-copper deposit, Western Tianshan, NW China: Constraints from (U-Th)/He and fission-track thermochronology. Ore Geology Reviews, https://doi.org/10.1016/j.oregeorev.2022.105220.

Sun, S.S., and McDonough, W.F. 1989. Chemical and isotopic systematics of oceanic basalts: implications for mantle composition and processes. Geological Society, London, Special Publications, 42, 313-345

Tan, Z., Xiao, W.J., Mao, Q.G., Wang, H., Sang, M., Li, R., Gao, L.M., Guo, Y.H., Gan, J.M, Liu, Y.H., Wan, B., 2022. Final closure of the Paleo Asian Ocean basin in the early Triassic. Communications Earth & Environment, https://doi.org/10.1038/s43247-022-00578-4.

Tang, G.J., Wang, Q., Wyman, D.A., Sun, M., Zhao, Z.H., and Jiang, Z.Q. 2013. Petrogenesis of gold-mineralized magmatic rocks of the Taerbieke area, northwestern Tianshan (western China): Constraints from geochronology, geochemistry and Sr–Nd–Pb–Hf isotopic compositions. Journal of Asian Earth Sciences, 74, 113–128, https://doi.org/10.1016/j.jseaes.2013.03.022

Turner, W., Richards, J., Nesbitt, B., Muehlenbachs, K., and Biczok, J. 2001. Proterozoic low-sulfidation epithermal Au-Ag mineralization in the Mallery Lake area, Nunavut, Canada. Mineralium Deposita, 36, 442–457, https://doi.org/10.1007/s001260100181

Vavra, G. 1994. Systematics of internal zircon morphology in major Variscan granitoid types. Contributions to Mineralogy and Petrology, 117, 331–344, https://doi.org/10.1007/BF00307269

Vermeesch, P. 2018. IsoplotR: A free and open toolbox for geochronology. Geoscience Frontiers, 9, 1479-1493, https://doi.org/10.1016/j.gsf.2018.04.001

Völkening, J., Walczyk, T., and Heumann, K.G., 1991, Osmium isotope ratio determinations by negative thermal ion mass spectrometry. International Journal of Mass Spectrometry Ion Processes, 105, 147–159

Wang, Z.X., Wu, J.Y., Lu, X.C., Zhang, J.G., and Liu, C.D. (eds) 1990. Polycyclic Tectonic Evolution and Metallogeny of the Tianshan Mountains. Science Press, Beijing

Wang, B., Cluzel, D., Shu, L., Faure, M., Charvet, J., Chen, Y., Meffre, S., and de Jong, K. 2009. Evolution of calc-alkaline to alkaline magmatism through Carboniferous convergence to Permian transcurrent tectonics, western Chinese Tianshan. International Journal of Earth Sciences, 98, 1275–1298, https://doi.org/10.1007/s00531-008-0408-y

Wang, Y.N., Cai, K.D., Sun, M., Xiao, W.J., De Grave, J., Wan, B., and Bao, Z.H. 2018. Tracking the multi-stage exhumation history of the western Chinese Tianshan by Apatite Fission Track (AFT) dating: implication for the preservation of epithermal deposits in the ancient orogenic belt. Ore Geology Reviews, 100, 111–132, https://doi.org/10.1016/j.oregeorev.2017.04.011

Wang, Y.N., Cai, K.D., Sun, M., and Bao, Z.H. 2021. Burial and exhumation of late Paleozoic arc-related rocks in the Tulasu basin, Western Chinese Tianshan: Implication for the preservation of epithermal deposits in old orogenic belts. Gondwana Research, 97, 51–67, https://doi.org/10.1016/j.gr.2021.05.010

Wei, J.L., Cao, X.Z., Xu, B.J., Zhang, W.S., Rao, D.P., and Huang, L.W. 2014. Erosion and post-mineralization change of Axi epithermal gold deposit in Western Tianshan Mountains. Mineral Deposits, 33, 241–254 (in Chinese with English abstract).

White, N.C., and Hedenquist, J.W. 1990. Epithermal environments and styles of mineralization - variations and their causes, and guidelines for exploration. Journal of Geochemical Exploration, 36, 445–474, https://doi.org/10.1016/0375-6742(90)90063-G

Wilkinson, B. H., and Kesler, S. E. 2007. Tectonism and exhumation in convergent margin orogens: Insights from ore deposits. Journal of Geology, 115, 611–627, https://doi.org/10.1086/521606

Wolf, R., Farley, K., and Kass, D.J.C.G. 1998. A sensitivity analysis of the apatite (U-Th-[Sm])/He thermochronometer. Chemical Geology, 148, 105–114.

Xia, L.Q., Xu, X.Y., Xia, Z.C., Li, X.M., Ma, Z.P., and Wang, L.S. 2004. Petrogenesis of Carboniferous rift-related volcanic rocks in the Tianshan, northwestern China. Geological Society of America Bulletin, 116, 419–433 https://doi.org/10.1130/B25243.1

Xiao, W.J., and Kusky, T. 2009, Geodynamic processes and metallogenesis of the Central Asian and related orogenic belts. Gondwana Research, 16, 167–169. https://doi.org/10.1016/j.gr.2009.05.001

Xiao, W.J., Windley, B.F., Huang, B.C., Han, C.M., Yuan, C., Chen, H.L., Sun, M., Sun, S., and Li, J.L. 2009. End-Permian to mid-Triassic termination of the accretionary processes of the southern Altaids: implications for the geodynamic evolution, Phanerozoic continental growth and metallogeny of Central Asia. International Journal of Earth Sciences, 98, 1189–1217. https://doi.org/10.1007/s00531-008-0407-z

Xiao, W.J, Windley, B.F., Allen, M.B., and Han, C.M. 2013. Paleozoic multiple accretionary and collisional tectonics of the Chinese Tianshan orogenic collage. Gondwana Research, 23, 1316–1341, https://doi.org/10.1016/j.gr.2012.01.012

Xiao, W.J, Song, D.F., Windley, B.F., Li, J.L., Han, C.M., Wan, B., Zhang, J.E., Ao, S.J., and Zhang, Z.Y. 2019. Research progresses of the accretionary processes and metallogenesis of the Central Asian Orogeni Belt. Science China Earth Sciences, https://doi.org/10.1007/s11430-019-9524-6

Xu, X., Li, X., Ma, Z., Xia, L., and Peng, S. 2006. LA-ICPMS zircon U-Pb dating of gabbro from the Bayingou ophiolite in the northern Tianshan Mountains. Acta Geologica Sinica, 80, 1168–1176 (in Chinese with English abstract)

Ye, T., Xi, W., Li, N., and Danisk, M. 2020. From magma replenishment to epithermal mineralization: Combined evidence from zircon U-Pb, (U-Th-[Sm])/He and trace element data. Ore Geology Reviews, https://doi.org/10.1016/j.oregeorev.2020.103746.

Yuan, H.L., Gao, S., Dai, M.N., Zong, C.L., Guenther, D., Fontaine, G. H., Liu, X.M., and Diwu, C. 2008. Simultaneous determinations of U-Pb age, Hf isotopes and trace element compositions of zircon by excimer laser-ablation quadrupole and multiple-collector ICP-MS. Chemical Geology, 247, 100-118, http:// doi.org/10.1016/j.chemgeo.2007.10.003.

Yu, X.Q., Wang, Z.X., Zhou, X., Xiao, W.F. and Yang, X.P. 2016. Zircon U-Pb geochronology and Sr-Nd isotopes of volcanic rocks from the Dahalajunshan Formation: implications for Late Devonian-Middle Carboniferous tectonic evolution of the Chinese Western Tianshan. International Journal of Earth Sciences, 105, 1637–1661, https://doi.org/10.1007/s00531-015-1275-y

Yu, J., Li, N., Qi, N., Guo, J.P., and Chen, Y.J. 2018. Carboniferous-Permian tectonic transition envisaged in two magmatic episodes at the Kuruer Cu-Au deposit, Western Tianshan (NW China). Journal of Asian Earth Sciences, 153, 395–411, https://doi.org/10.1016/j.jseaes.2017.07.048

Zhai, W., Sun, X., Gao, J., He, X., Liang, J., Miao, L., and Wu, Y. 2006. SHRIMP dating of zircons from volcanic host rocks of Dahalajunshan Formation in Axi gold deposit, Xinjiang, China, and its geological implications. Acta Petrologica Sinica, 22, 1399−1404 (in Chinese with English abstract).

Zhai, W., Sun, X.M., Sun, W.D., Su, L.W., He, X.P., and Wu, Y.L. 2009. Geology, geochemistry, and genesis of Axi: A Paleozoic low-sulfidation type epithermal gold deposit in Xinjiang, China. Ore Geology Reviews, 36, 265−281, https://doi.org/10.1016/j.oregeorev.2009.04.003

Zhang, B. 2020. Metallogeny study of the Axi gold deposit in Western Tianshan, Xinjiang. Ph.D thesis, Peking University, Beijing (in Chinese with English abtract).

Zhang, B., Li, N., Shu, S., Wang, W., Yu, J., Chen, X., Ye, T., and Chen, Y. 2018. Textural and compositional evolution of Au-hosting Fe-S-As minerals at the Axi epithermal gold deposit, Western Tianshan, NW China. Ore Geology Reviews, 100, 31−50, https://doi.org/10.1016/j.oregeorev.2017.08.002

Zhao, X. B., Xue, C. J., Men, Q., Yan, Y., Wang, H., Zu, B., Mi, D., and Li, X. 2014a. Origin and metallogenesis of the Tawuerbieke gold deposit, western Tianshan: Insight from Re-Os geochronology and S-Pb isotopic compositions. Earth Science Frontiers, 21, 176−186 (in Chinese with English abstract).

Zhao, X.B., Xue, C. J., Symons, D.T.A., Zhang, Z., and Wang, H. 2014b. Microgranular enclaves in island-arc andesites: A possible link between known epithermal Au and potential porphyry Cu-Au deposits in the Tulasu ore cluster, western Tianshan, Xinjiang, China. Journal of Asian Earth Sciences, 85, 210–223, https://doi.org/10.1016/j.jseaes.2014.01.014

Zhao, X.B., Xue, C. J., Seltmann, R., Dolgopolova, A., Andersen, Jens C.O, and Zhang, G.Z. 2020.

Volcanic-plutonic connection and associated Au-Cu mineralization of the Tulasu ore district, Western Tianshan, NW China: Implications for mineralization potential in Palaezoic arc terranes. Geological Journal, 55: 2318-2341, https://doi.org/10.1002/gj.3750

Zhao, X.B., Xue, C. J., Zhao, W.C., Seltmann, R., Symons, D.T.A., Dolgopolova, A., and Zhang, Y. 2021. Cooling and exhumation of the Late Paleozoic Tulasu epithermal gold system, Western Tianshan, NW China: Implications for preseration of Pre-Mesozoic epithermal deposits. Journal of the Geological Society, https://doi.org/10.1144/jgs2020-099

Zhu, Y., Guo, X., Song, B., Zhang, L., and Gu, L. 2009. Petrology, Sr-Nd-Hf isotopic geochemistry and zircon chronology of the Late Palaeozoic volcanic rocks in the southwestern Tianshan Mountains, Xinjiang, NW China. Journal of the Geological Society, 166,1085-1099, https://doi.org/10.1144/0016-76492008-130

Figure captions

Fig.1. (a) Sketch map of the Central Asian Orogenic Belt, showing the location of the Chinese Western Tianshan; (b) Geological map of the Chinese Western Tianshan (modified after Tang et al., 2013); (c) Cross section along the Yili Block (A-A’), showing the location of the Tulasu Basin and the epithermal gold deposit it hosted (cited from Wang et al., 2018).

In Fig. 1b, numbers in circle refer to the tectonic boundaries: ① the North Tianshan (or called the Northern Central Tianshan) suture zone, ② the Nikolaev Line-North Nalati suture zone and ③ the South Tianshan (or Southern Central Tianshan) suture zone. In Fig. 1c, the magnitude of vertical exaggeration along the profile is 1:100000.

Fig. 2. Geological map (a) and stratigraphic column (b) of the Tulasu Basin (modified after Zhai et al., 2009; Zhao et al., 2014a, b; Wang et al., 2018).

Fig. 3. (a) Geological map of the Axi gold deposit (modified after Dong and Sha, 2005; Zhai et al., 2009); (b) cross section along the A-A′ prospecting line in Fig. a, showing the basal conglomerate orebody hosted by the Aqialehe Formation and the epithermal gold orebodies hosted by the Dahalajunshan Formation (modified after Wei et al. 2014); (c) the spatial relationship between the basal conglomerate-style gold orebody and epithermal gold orebody (provided by the Western Gold Yili Co. Ltd.).

Fig. 4. Representative zircons CL images, exhibiting the internal structure of two types of zircons.

Fig. 5. Box plots of Hf (a), U (b), $(Yb/Gd)_N$ (c) and Ti-in-zircon temperature (d) showing the difference between Zr1 and Zr2. Data are cited from Appendix Table S1, the chondrite values are cited from Sun and McDonough (1989).

Abbreviation: And, andesite; Am And, amphibole andesite; Cpx And: pyroxene andesite; Qz And: quartz andesite

Fig. 6. Cumulative plot of $^{206}Pb/^{238}U$ ages for four andesitic rocks (a-d), arranged in order of consecutive age and differentiated into different groups, combined with a probability plot (a-e) and the weighted mean age for the youngest group (f).

The flat regions in the cumulative plot correspond to a significant peak in the probability plot, which is considered to represent a specific geological event. The weighted mean age is calculated, in some cases including analyses from zircon belonging to different types. Older outliers (>370 Ma) are omitted in this plot. Data are cited from Table S2.

Fig. 7. Age-elevation relationship for the apatite (U-Th-[Sm])/He data (central ages are shown with uncertainties and single grain AHe ages without uncertainties for clarity purposes).

Data are cited from Table 3.

Abbreviation: And, andesite; Am And, amphibole andesite; Cpx And: pyroxene andesite; Qz And: quartz andesite.

Fig. 8. Pyrite Re-Os isochron (a) and weighted mean model age (b) for the Axi gold deposit. See text for discussion. Data are reported in Table 4.

Fig. 9 Thermal history modelling of sample AX39

Fig. 10. Time–temperature histories for the Axi gold deposit

Data are cited from Table 1.

Note: here we attribute the first gold mineralization event to 350 °C (producing coarse-grained pyrite) whereas the second one (forming epithermal mineralization and fine-grained pyrite) to 300 °C.

Table

Table 1 Chronological data for the Axi deposit

Table 2 Samples used for chronological study

Table 3 Zircon and apatite (U–Th)/He thermochronology results for andesitic rocks at the Axi gold deposit

Table 4 Re and Os data synopsis of pyrite and marcasite from the Axi epithermal gold deposit

Appendix

Fig. S1 Th/U vs. Ti-in-zircon (a), Th/U vs. Hf (b) and the changes of Hf (c) and Ti-in-zircon (d) along with $^{206}Pb/^{238}U$ ages.

Table S1 Trace element data (ppm) of the dated zircons collected from andesitic rocks

Table S2 LA-ICPMS zircon U-Pb data for andesitic host at the Axi gold deposit

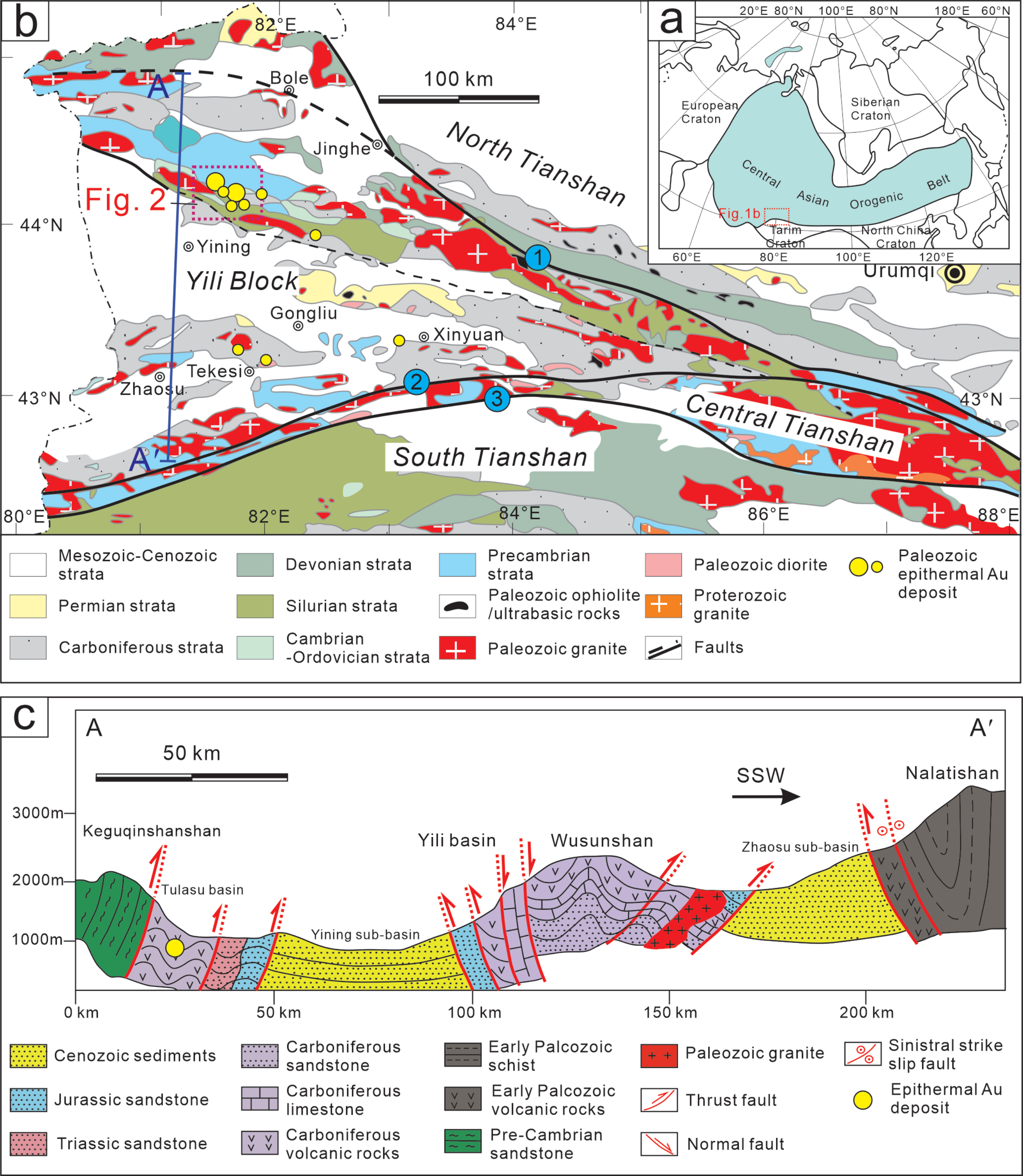
b
a
82°E
84°E
Bole
100 km
A
Jinghe
North Tianshan
Fig. 2
44°N
Yining
Yili Block
Gongliu
Xinyuan
Tekesi
Zhaosu
43°N
Central Tianshan
South Tianshan
A'
80°E
82°E
84°E
86°E
88°E
Urumqi
20°E 80°N 100°E 80°N 180°E 60°N
European Craton
Siberian Craton
Central Asian Orogenic Belt
Fig.1b
Tarim Craton
North China Craton
60°E 80°E 100°E 120°E
Mesozoic-Cenozoic strata
Permian strata
Carboniferous strata
Devonian strata
Silurian strata
Cambrian -Ordovician strata
Precambrian strata
Paleozoic ophiolite /ultrabasic rocks
Paleozoic granite
Paleozoic diorite
Proterozoic granite
Faults
Paleozoic epithermal Au deposit
c
A
A′
50 km
SSW
Nalatishan
3000m
2000m
1000m
Keguqinshanshan
Tulasu basin
Yining sub-basin
Yili basin
Wusunshan
Zhaosu sub-basin
0 km
50 km
100 km
150 km
200 km
Cenozoic sediments
Jurassic sandstone
Triassic sandstone
Carboniferous sandstone
Carboniferous limestone
Carboniferous volcanic rocks
Early Palcozoic schist
Early Palcozoic volcanic rocks
Pre-Cambrian sandstone
Paleozoic granite
Thrust fault
Normal fault
Sinistral strike slip fault
Epithermal Au deposit

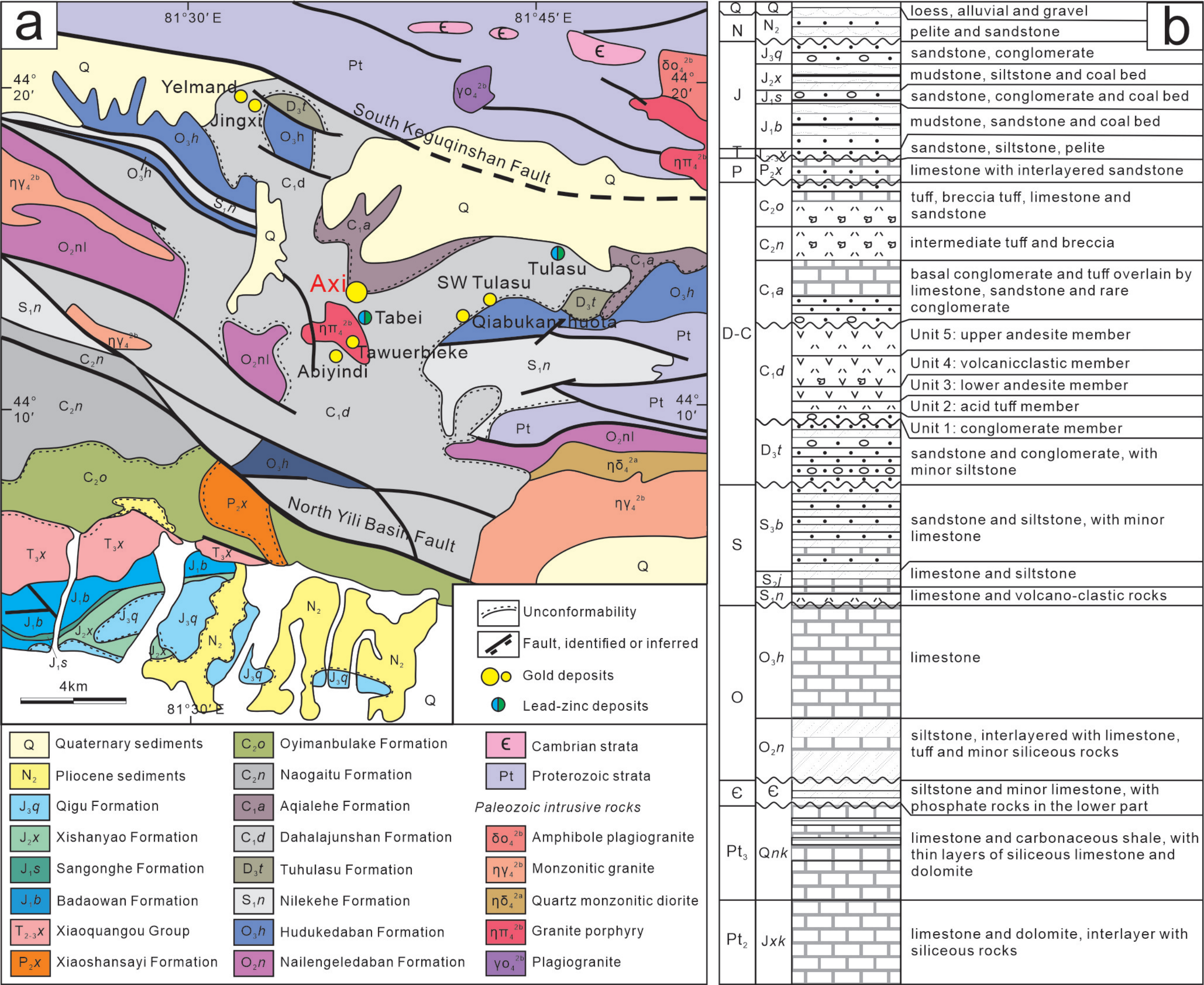
a
81°30′ E
81°45′ E
44° 20′
44° 10′
Yelmand
Jingxi
South Keguqinshan Fault
Axi
Tabei
Tawuerbieke
Abiyindi
SW Tulasu
Tulasu
Qiabukanzhuota
North Yili Basin Fault
4km
81°30′ E
Unconformability
Fault, identified or inferred
Gold deposits
Lead-zinc deposits
Q Quaternary sediments
N2 Pliocene sediments
J3q Qigu Formation
J2x Xishanyao Formation
J1s Sangonghe Formation
J1b Badaowan Formation
T2-3x Xiaoquangou Group
P2x Xiaoshansayi Formation
C2o Oyimanbulake Formation
C2n Naogaitu Formation
C1a Aqialehe Formation
C1d Dahalajunshan Formation
D3t Tuhulasu Formation
S1n Nilekehe Formation
O3h Hudukedaban Formation
O2n Nailengeledaban Formation
Ꞓ Cambrian strata
Pt Proterozoic strata
Paleozoic intrusive rocks
δο4 2b Amphibole plagiogranite
ηγ4 2b Monzonitic granite
ηδ4 2a Quartz monzonitic diorite
ηπ4 2b Granite porphyry
γο4 2b Plagiogranite
b
Q Q loess, alluvial and gravel
N N2 pelite and sandstone
J J3q sandstone, conglomerate
J2x mudstone, siltstone and coal bed
J1s sandstone, conglomerate and coal bed
J1b mudstone, sandstone and coal bed
T T2-3x sandstone, siltstone, pelite
P P2x limestone with interlayered sandstone
D-C C2o tuff, breccia tuff, limestone and sandstone
C2n intermediate tuff and breccia
C1a basal conglomerate and tuff overlain by limestone, sandstone and rare conglomerate
C1d Unit 5: upper andesite member
Unit 4: volcanicclastic member
Unit 3: lower andesite member
Unit 2: acid tuff member
Unit 1: conglomerate member
D3t sandstone and conglomerate, with minor siltstone
S S3b sandstone and siltstone, with minor limestone
S2j limestone and siltstone
S1n limestone and volcano-clastic rocks
O O3h limestone
O2n siltstone, interlayered with limestone, tuff and minor siliceous rocks
Ꞓ Ꞓ siltstone and minor limestone, with phosphate rocks in the lower part
Pt3 Qnk limestone and carbonaceous shale, with thin layers of siliceous limestone and dolomite
Pt2 Jxk limestone and dolomite, interlayer with siliceous rocks

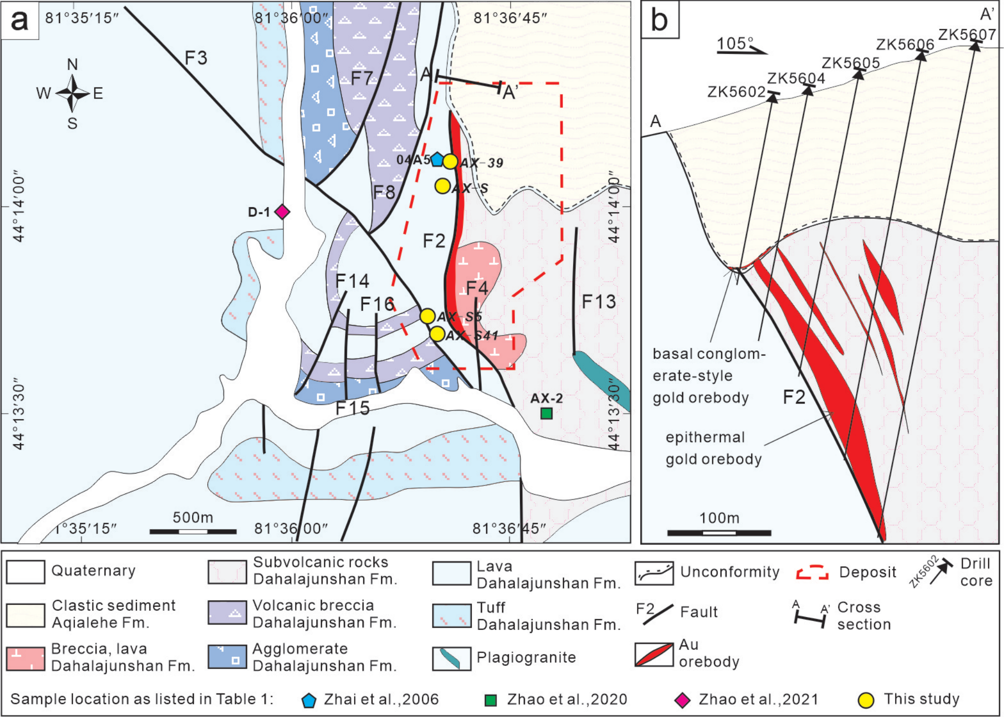

a
81°35′15″
81°36′00″
81°36′45″
N
S
W
E
F3
F7
F8
F2
F4
F13
F14
F16
F15
A
A'
04A5
AX-39
AX-S
AX-S5
AX-S41
AX-2
D-1
44°14′00″
44°13′30″
500m
b
105°
ZK5602
ZK5604
ZK5605
ZK5606
ZK5607
basal conglom-
erate-style
gold orebody
epithermal
gold orebody
100m
Quaternary
Clastic sediment Aqialehe Fm.
Breccia, lava Dahalajunshan Fm.
Subvolcanic rocks Dahalajunshan Fm.
Volcanic breccia Dahalajunshan Fm.
Agglomerate Dahalajunshan Fm.
Lava Dahalajunshan Fm.
Tuff Dahalajunshan Fm.
Plagiogranite
Unconformity
Fault
Au orebody
Deposit
Cross section
Drill core
Sample location as listed in Table 1:
Zhai et al.,2006
Zhao et al.,2020
Zhao et al.,2021
This study

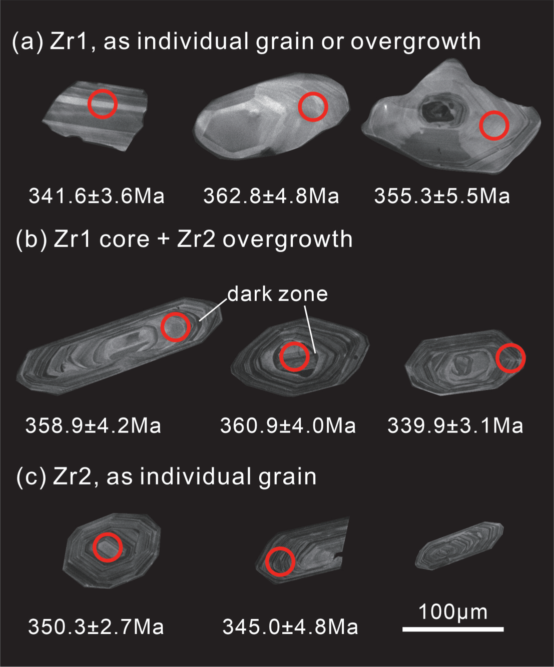
(a) Zr1, as individual grain or overgrowth
341.6±3.6Ma
362.8±4.8Ma
355.3±5.5Ma
(b) Zr1 core + Zr2 overgrowth
dark zone
358.9±4.2Ma
360.9±4.0Ma
339.9±3.1Ma
(c) Zr2, as individual grain
350.3±2.7Ma
345.0±4.8Ma
100μm

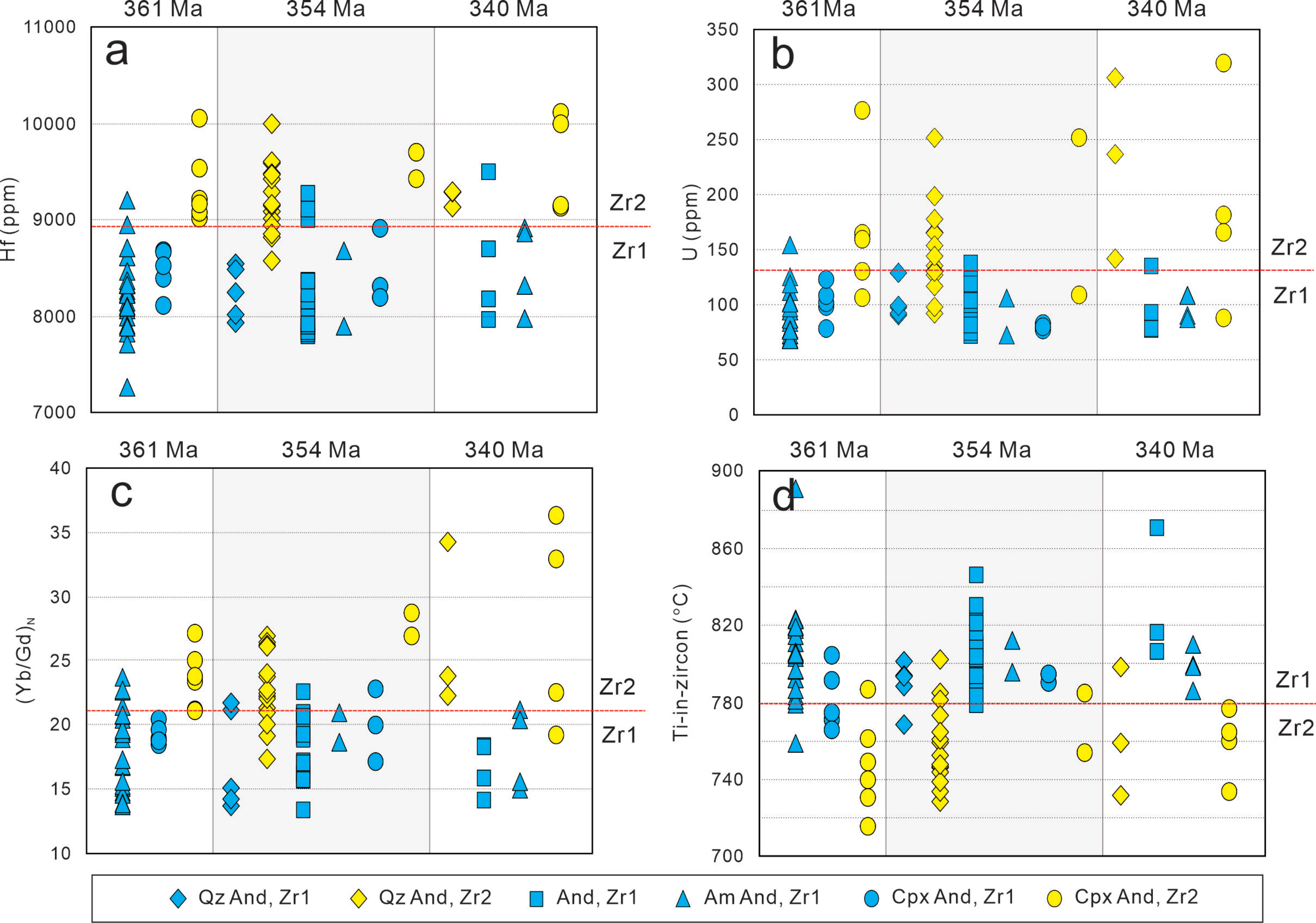

361 Ma
354 Ma
340 Ma
a
Hf (ppm)
Zr2
Zr1
b
U (ppm)
c
(Yb/Gd)N
d
Ti-in-zircon (°C)
Qz And, Zr1
Qz And, Zr2
And, Zr1
Am And, Zr1
Cpx And, Zr1
Cpx And, Zr2

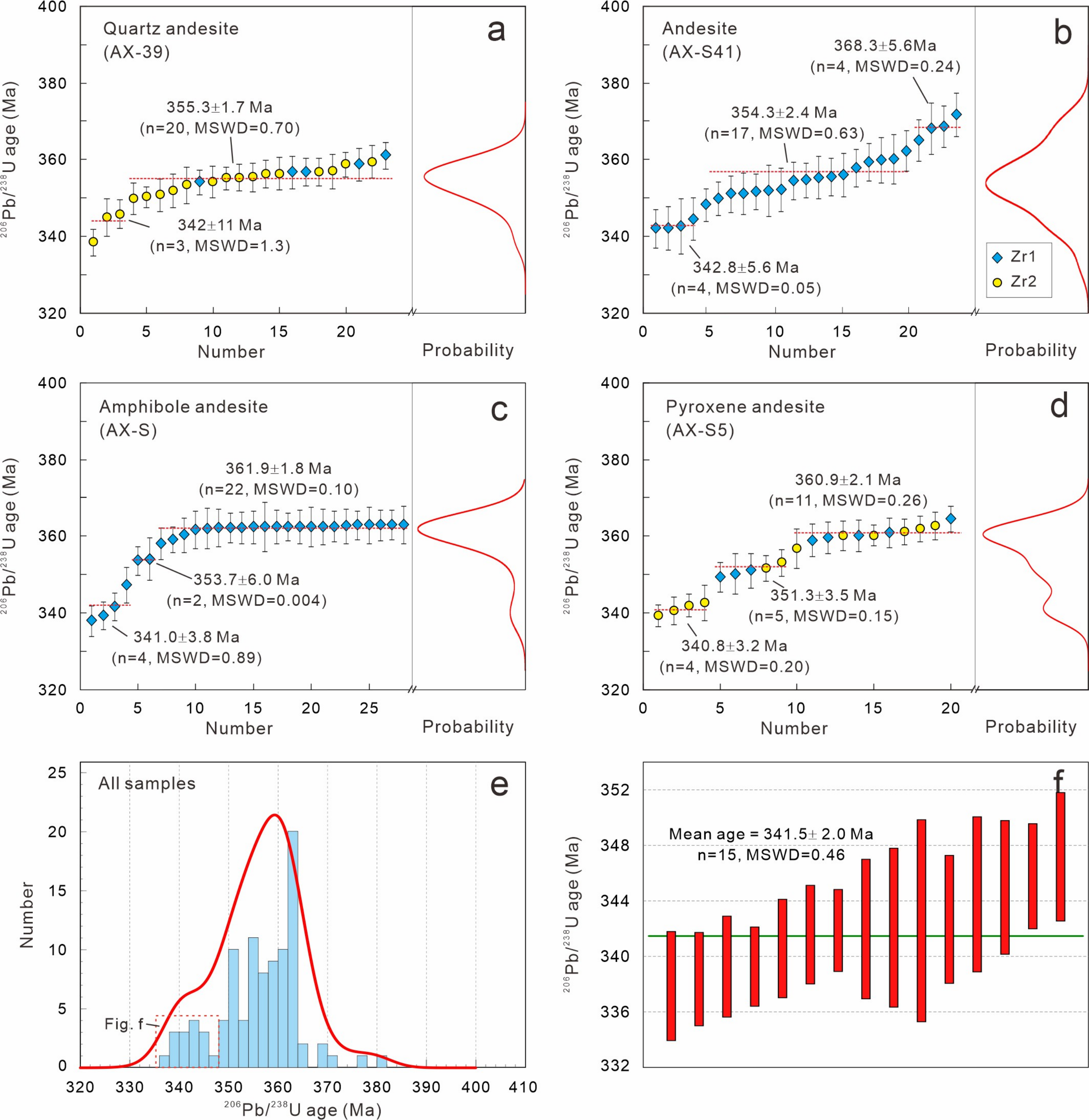

Quartz andesite
(AX-39)
a
355.3±1.7 Ma
(n=20, MSWD=0.70)
342±11 Ma
(n=3, MSWD=1.3)
Andesite
(AX-S41)
b
368.3±5.6Ma
(n=4, MSWD=0.24)
354.3±2.4 Ma
(n=17, MSWD=0.63)
342.8±5.6 Ma
(n=4, MSWD=0.05)
Zr1
Zr2
Amphibole andesite
(AX-S)
c
361.9±1.8 Ma
(n=22, MSWD=0.10)
353.7±6.0 Ma
(n=2, MSWD=0.004)
341.0±3.8 Ma
(n=4, MSWD=0.89)
Pyroxene andesite
(AX-S5)
d
360.9±2.1 Ma
(n=11, MSWD=0.26)
351.3±3.5 Ma
(n=5, MSWD=0.15)
340.8±3.2 Ma
(n=4, MSWD=0.20)
206Pb/238U age (Ma)
Number
Probability
All samples
e
Fig. f
f
Mean age = 341.5± 2.0 Ma
n=15, MSWD=0.46

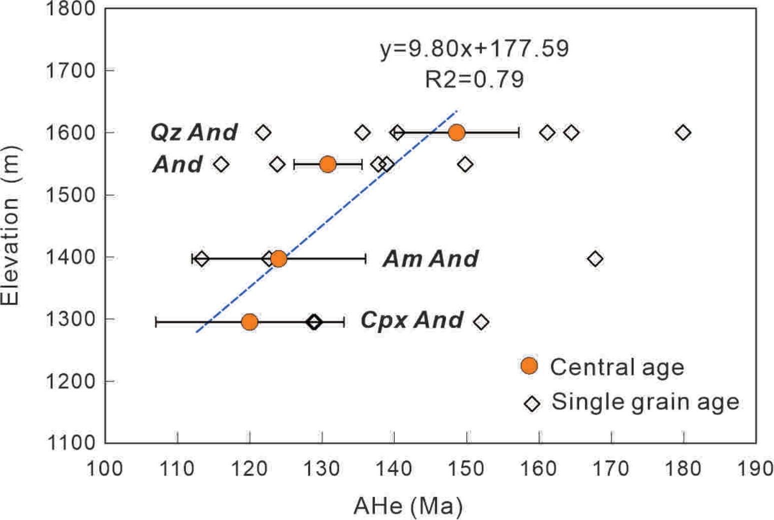

y=9.80x+177.59
R2=0.79
Qz And
And
Am And
Cpx And
Central age
Single grain age
Elevation (m)
AHe (Ma)
1800
1700
1600
1500
1400
1300
1200
1100
100
110
120
130
140
150
160
170
180
190

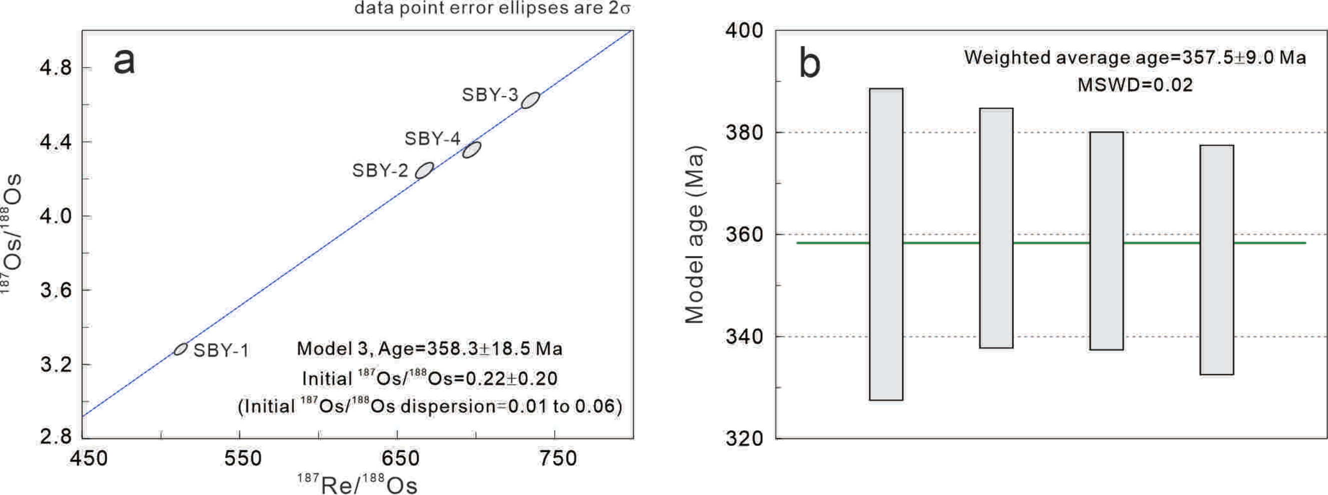
data point error ellipses are 2σ
a
4.8
4.4
4.0
3.6
3.2
2.8
187Os/188Os
450
550
650
750
187Re/188Os
SBY-3
SBY-4
SBY-2
SBY-1
Model 3, Age=358.3±18.5 Ma
Initial 187Os/188Os=0.22±0.20
(Initial 187Os/188Os dispersion=0.01 to 0.06)
b
400
380
360
340
320
Model age (Ma)
Weighted average age=357.5±9.0 Ma
MSWD=0.02

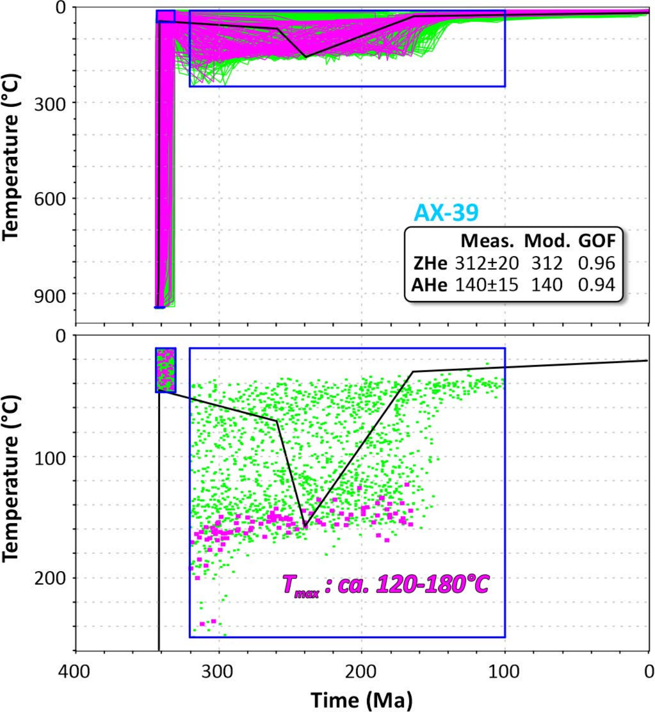

AX-39
Meas. Mod. GOF
ZHe 312±20 312 0.96
AHe 140±15 140 0.94
Temperature (°C)
0
300
600
900
Temperature (°C)
0
100
200
Tmax : ca. 120-180°C
400
300
200
100
0
Time (Ma)

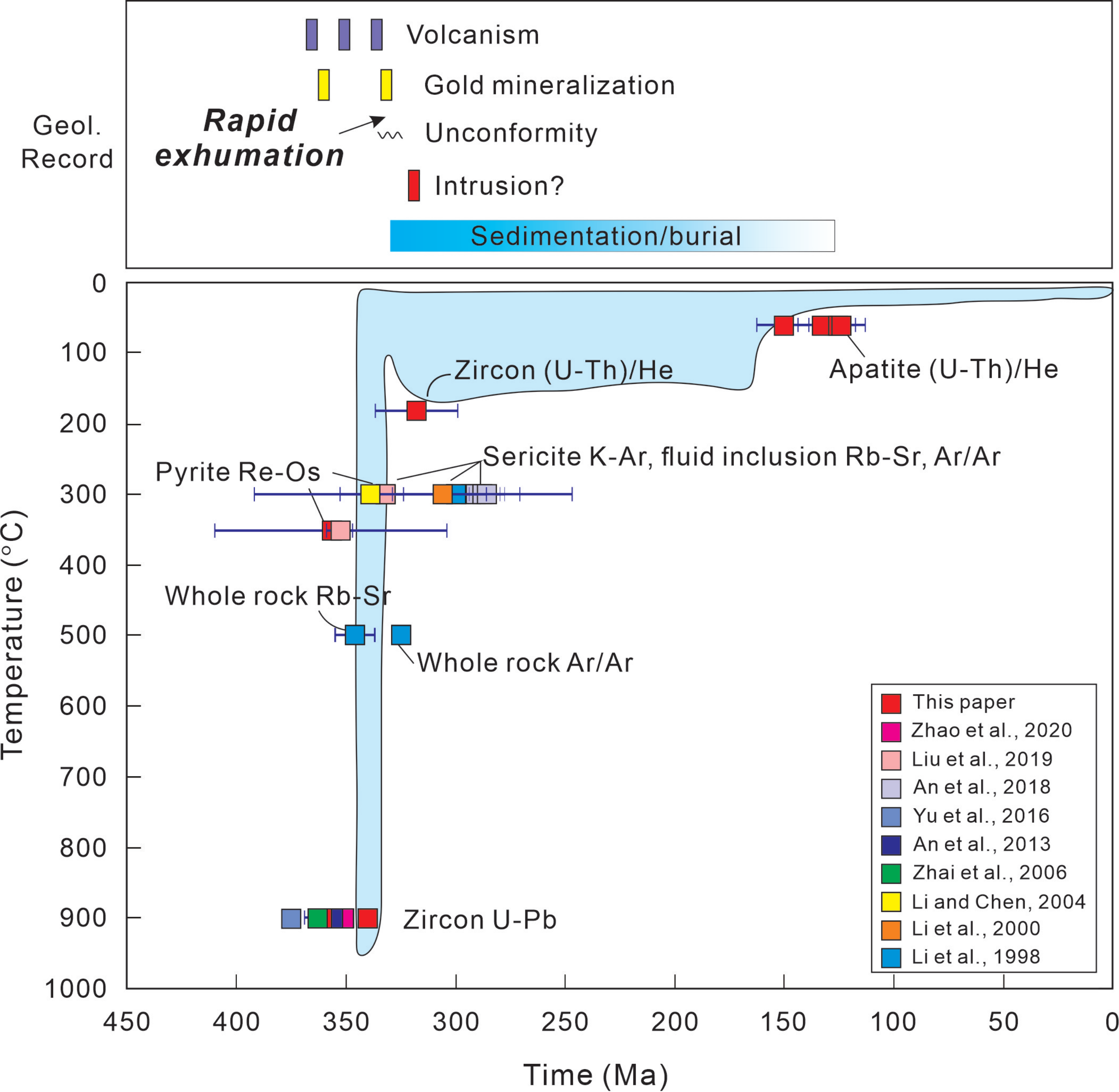

Volcanism
Gold mineralization
Rapid exhumation
Unconformity
Geol. Record
Intrusion?
Sedimentation/burial
Zircon (U-Th)/He
Apatite (U-Th)/He
Sericite K-Ar, fluid inclusion Rb-Sr, Ar/Ar
Pyrite Re-Os
Whole rock Rb-Sr
Whole rock Ar/Ar
Zircon U-Pb
This paper
Zhao et al., 2020
Liu et al., 2019
An et al., 2018
Yu et al., 2016
An et al., 2013
Zhai et al., 2006
Li and Chen, 2004
Li et al., 2000
Li et al., 1998
Temperature (°C)
Time (Ma)
0
100
200
300
400
500
600
700
800
900
1000
450
400
350
300
250
200
150
100
50
0